Cell Reports
Medicine

Article

A p38 MAPK-ROS axis fuels proliferation stress and DNA damage during CRISPR-Cas9 gene editing in hematopoietic stem and progenitor cells

Graphical abstract

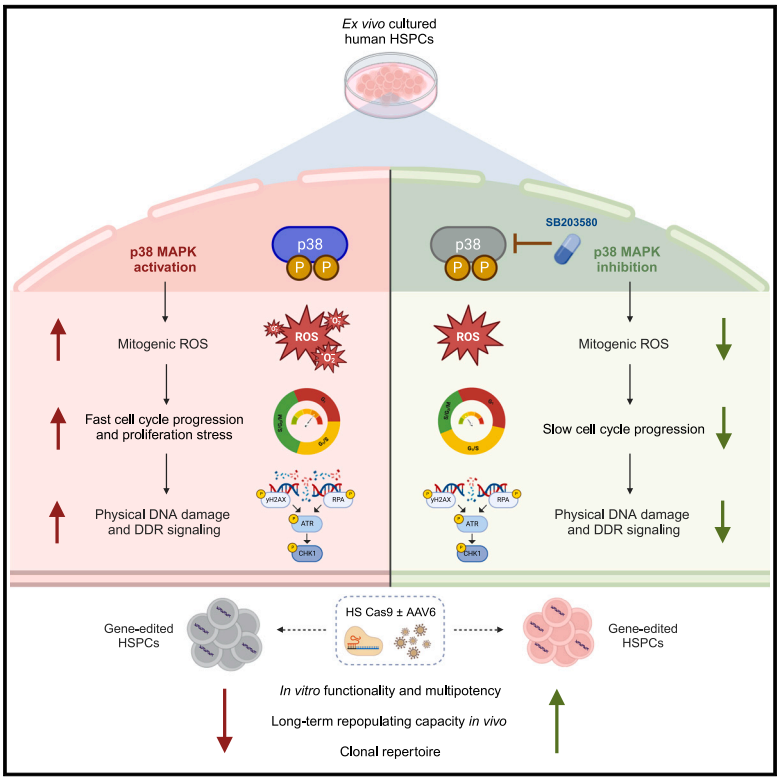

Highlights

- Shortening HSPC pre-stimulation reduces DDR-mediated responses to gene editing
- p38 MAPK-ROS induce fast cell-cycle progression fueling DNA damage and DDR signaling
- Preventing p38 activity mitigates proliferative stress and improves HSC fitness
- p38 inhibition enhances polyclonal and long-term reconstitution of edited HSPCs

Authors

Lucrezia della Volpe, Federico Midena, Roberta Vacca, ..., Anna Villa, Luigi Naldini, Raffaella Di Micco

Correspondence

dimicco.raffaella@hsr.it

In brief

Although detrimental, *ex vivo* activation of hematopoietic stem cells is required for gene editing strategies. Here, della Volpe et al. uncover a p38 MAPK-dependent molecular axis causing functional decline of gene-edited cells. Temporary p38 inhibition enhances the fitness of engineered cells for more effective and safer clinical applications.

della Volpe et al., 2024, Cell Reports Medicine *5*, 101823
November 19, 2024
https://doi.org/10.1016/j.xcrm.2024.101823

CellPress

Cell Reports Medicine

CellPress
OPEN ACCESS

Article

A p38 MAPK-ROS axis fuels proliferation stress and DNA damage during CRISPR-Cas9 gene editing in hematopoietic stem and progenitor cells

Lucrezia della Volpe,[1,2,7] Federico Midena,[1,2,7] Roberta Vacca,[1,2,7] Teresa Tavella,[1] Laura Alessandrini,[1,2] Giacomo Farina,[1,3] Chiara Brandas,[1] Elena Lo Furno,[1] Kety Giannetti,[1] Edoardo Carsana,[1] Matteo M. Naldini,[1,2] Matteo Barcella,[1] Samuele Ferrari,[1] Stefano Beretta,[1] Antonella Santoro,[1] Simona Porcellini,[1] Angelica Varesi,[1] Diego Gilioli,[1,2] Anastasia Conti,[1] Ivan Merelli,[4] Bernhard Gentner,[1,5] Anna Villa,[1,4] Luigi Naldini,[1,2] and Raffaella Di Micco[1,6,8,9,*]

[1]San Raffaele Telethon Institute for Gene Therapy (SR-Tiget), IRCCS San Raffaele Scientific Institute, 20132 Milan, Italy
[2]Vita-Salute San Raffaele University, 20132 Milan, Italy
[3]University of Milan-Bicocca, 20126 Milan, Italy
[4]National Research Council, Institute for Biomedical Technologies, 20054 Segrate, Italy
[5]Ludwig Institute for Cancer Research and Department of Oncology, University of Lausanne (UNIL) and Lausanne University Hospital (CHUV), 1066 Lausanne, Switzerland
[6]University School of Advanced Studies IUSS, 27100 Pavia, Italy
[7]These authors contributed equally
[8]X (formerly Twitter): @DiMiccoLab
[9]Lead contact
*Correspondence: dimicco.raffaella@hsr.it
https://doi.org/10.1016/j.xcrm.2024.101823

SUMMARY

Ex vivo activation is a prerequisite to reaching adequate levels of gene editing by homology-directed repair (HDR) for hematopoietic stem and progenitor cell (HSPC)-based clinical applications. Here, we show that shortening culture time mitigates the p53-mediated DNA damage response to CRISPR-Cas9-induced DNA double-strand breaks, enhancing the reconstitution capacity of edited HSPCs. However, this results in lower HDR efficiency, rendering *ex vivo* culture necessary yet detrimental. Mechanistically, *ex vivo* activation triggers a multi-step process initiated by p38 mitogen-activated protein kinase (MAPK) phosphorylation, which generates mitogenic reactive oxygen species (ROS), promoting fast cell-cycle progression and subsequent proliferation-induced DNA damage. Thus, p38 inhibition before gene editing delays G1/S transition and expands transcriptionally defined HSCs, ultimately endowing edited cells with superior multi-lineage differentiation, persistence throughout serial transplantation, enhanced polyclonal repertoire, and better-preserved genome integrity. Our data identify proliferative stress as a driver of HSPC dysfunction with fundamental implications for designing more effective and safer gene correction strategies for clinical applications.

INTRODUCTION

Ex vivo hematopoietic stem and progenitor cell (HSPC)-based gene therapies (GTs) represent a revolutionary class of ''living medicines'' for treating various monogenic diseases, including immunodeficiencies, hereditary anemias, and metabolic disorders.[1,2] GT is a multi-step process encompassing the harvest of HSPCs, *ex vivo* culture, exposure to engineering reagents, and reinfusion into patients to ensure a life-long supply of corrected hematopoietic progeny. Specifically, functional genes can be inserted by gene transfer (through randomly integrating γRetroviral or Lentiviral vectors) or precisely restored by gene editing (GE) with programmable nucleases such as CRISPR-Cas9.[2–4] Nuclease-induced double-strand breaks (DSBs) can be sealed by the error-prone non-homologous end joining (NHEJ) pathway disrupting a faulty gene or repaired by the high-fidelity homology-directed repair (HDR)[5] occurring during the S and G2 phase of the cell cycle.[6] Currently, HDR remains the only option for long-range correction of disease-causing mutations by inserting a functional cDNA cassette, often delivered with an adenoviral-associated viral vector (AAV6). As HDR engagement in long-term repopulating hematopoietic stem cells (HSCs) requires cell-cycle activation,[7,8] current protocols consist of 48–72 h of pre-stimulation with a previously optimized combination of cytokines and stem-preserving factors to force exit from quiescence and ensure a sizable fraction of corrected primitive cells.[8–12]

We recently discovered that GE culminates into a p53-mediated DNA damage response (DDR) activation, leading to cell differentiation, loss of engraftment, and reduced graft clonality,[11–13] although whether these responses might be exacerbated by prolonged *ex vivo* culture remains to be established.

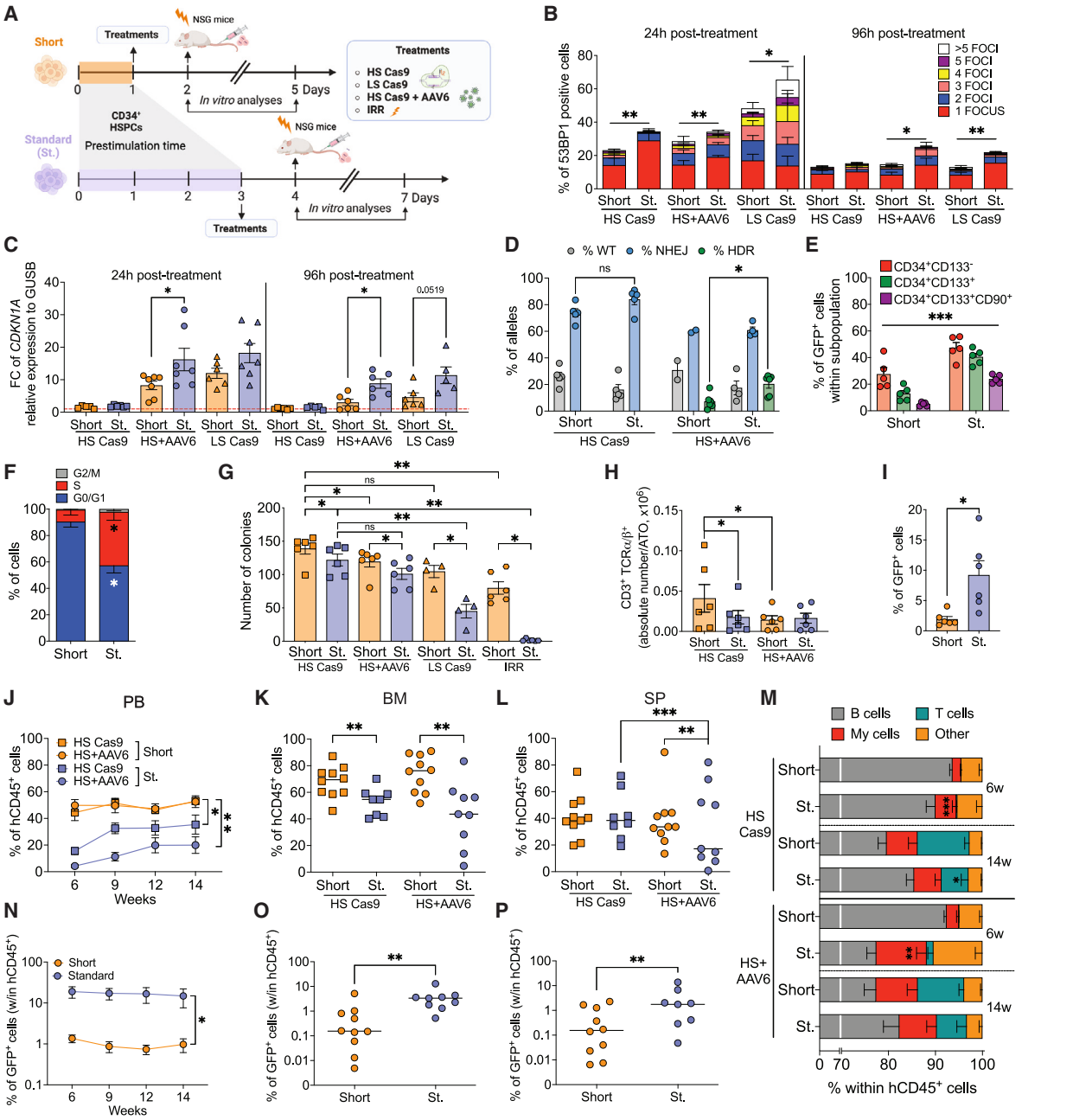

Figure 1. *Ex vivo* activation is a prerequisite for efficient HDR-based correction, although it heightens DDR activation and affects GE HSPC repopulation capacity

(A) Experimental workflow for short and standard protocols in human CB-derived HSPCs. Indicated treatments were performed at day 1 (short) or day 3 (standard) post-thawing, while *in vitro* analyses were conducted at 24 or 96 h post-treatments (corresponding to day 2 or 4, and day 5 or 7, respectively).

(B) 53BP1 foci distribution (24 h: n = 6,8,5,8,6,8; 96 h: n = 6, 6, 6, 4, 6, 7). Mann-Whitney test.

(C) Relative expression of *CDKN1A* (24 h: n = 5, 6, 7, 7, 6, 7; 96 h: n = 6, 5, 6, 6, 6, 5). For each time point, fold change was calculated relatively to HSPCs treated with an RNP loaded with a gRNA with no specificity against the human genome. Mann-Whitney test.

(D) Percentage of wild-type and HDR- or NHEJ-edited alleles measured 96 h post-editing (HS: n = 5; HS+AAV6: n = 2, 2, 6, 4, 4, 6). Wilcoxon test.

(E) Percentage of GFP$^+$ cells within HSPC subpopulations (CD34$^+$CD133$^-$, CD34$^+$CD133$^+$, and CD34$^+$CD133$^+$CD90$^+$ cells) at 96 h post-treatments (n = 5). Kruskal-Wallis test.

(F) Percentage of HSPCs in indicated cell-cycle phases measured at day 1 (short: n = 5) and day 3 (standard: n = 4). Mann-Whitney test.

(G) Number of colonies generated by HSPCs plated at 96 h post-treatment (HS Cas9: n = 6; HS+AAV6: n = 6; LS Cas9: n = 4; IRR: n = 6). Wilcoxon test for intra-treatment comparisons or Mann-Whitney test for inter-treatment measurements.

(H) Absolute number of CD3$^+$TCRα/β^+ cells in ATO seeded with HSPCs after the indicated treatment (n = 6). Wilcoxon test.

(legend continued on next page)

Previous studies reported that similar detrimental consequences may be due to the accumulation of reactive oxygen species (ROS) and activation of the p38 mitogen-activated protein kinase (MAPK) resulting in differentiation and loss of HSC self-renewal,[14–16] which could be counteracted by p38 inhibition,[17,18] leading to the assumption that ROS may directly act as pro-differentiating molecules on HSPCs.

Here, we identified a molecular axis where p38 MAPK-induced ROS act primarily as mitogenic molecules that alter HSPC cell-cycle dynamics, ultimately converging in proliferation-associated DNA damage accumulation and DDR activation. Importantly, p38 MAPK inhibition before GE mitigates culture stress by slowing down cell-cycle kinetics, preserving transcriptionally defined primitive HSCs, and enhancing the clonal output of edited HSPCs in the long term.

RESULTS

Ex vivo culture increases DDR burden and affects the functionality of genetically engineered human HSPCs

To study the contribution of *ex vivo* culture on HSPC response to nuclease-induced DSBs and viral vectors employed for long-range GE, we investigated the impact of DDR activation and DNA repair mechanisms in human HSPCs ($CD34^+$ cells) after an overnight recovery post-thawing ("short" protocol) or upon three days of pre-stimulation ("standard or St." protocol) (Figure 1A). HSPCs were nucleofected with Cas9 ribonucleoprotein complexes (RNPs) pre-assembled with guide RNA (gRNA)[19] previously reported to have no detectable off-targets (high specificity [HS Cas9], targeting the *AAVS1* safe harbor),[11,12] or more relaxed accuracy (low specificity Cas9 [LS Cas9], targeting *IL2RG*).[12] We also included cells treated with HS Cas9 in the presence of an AAV6 template for HDR integration of a GFP-expressing cassette (defined HS+AAV6) and low-dose irradiation (IRR) as a heightened load of DSBs and elevated DDR burden control (Figure 1A).

To investigate how *ex vivo* culture impacts HSPC proficiency to repair individual or multiple DSBs and activate p53-mediated DDR, we compared the accumulation and resolution of 53BP1 nuclear foci and *CDKN1A* (p21) levels across treatments. In line with our previous findings,[12] we reported an increased DDR burden when cells experienced the combination of HS and AAV6 or multiple DSBs by LS Cas9. Importantly, we observed a higher number of 53BP1 foci *per* cell and p21 levels in HSPCs edited with the standard protocol, reflecting higher vulnerability and protracted DDR activation, albeit changes in apoptosis were negligible (Figures 1B, 1C, S1A, and S1B). As persistency of DSBs during cell divisions may trigger genome instability phenomena, we analyzed the presence of micronuclei (MNs)-positive cells[20] and found a significant increase in MN-carrying cells across conditions after standard protocol, particularly in HS+AAV6 and LS Cas9 treatments (Figure S1C). Similarly, when we further increased the DNA damage load by IRR, the standard protocol displayed more DNA damage, reduced DNA repair proficiency, and higher p53-mediated DDR activation over time (Figures S1D and S1E).

We next evaluated on-target repair proficiency by NHEJ and HDR in HSPCs treated with the two clinically relevant conditions (HS Cas9 for gene disruption or HS+AAV6 for gene correction strategies). We found that, while NHEJ levels were comparable in all conditions, HDR efficiency was consistently lower across subsets in the short protocol (Figures 1D and 1E; see the gating strategy in Figure S1F), according to a reduced fraction of cells that progressed into the S phase of the cell cycle (Figure 1F).

For all conditions tested, we evaluated the clonogenic capacity and found that, according to the extent of DDR activation, short protocol-treated HSPCs showed an overall improved functionality (Figure 1G), especially for the myeloid output (Figure S1G). Moreover, we assessed the capacity of HSPCs edited with HS Cas9 and HS+AAV6 to differentiate along the lymphoid lineage in an innovative artificial thymic organoid (ATO) platform.[21] Thus, we reported increased output of $CD3^+TCR\alpha/\beta^+$ cells for HS Cas9 HSPCs of the short protocol and a reduction of $CD3^+TCR\alpha/\beta^+$ cells for HS+AAV6 conditions irrespective of the protocol employed (Figure 1H). Moreover, T cell-progenitor subsets were similar across all conditions, albeit with a modest reduction in early T cell precursors (ETPs) and pro-T cells (Pro-T) for the HS+AAV6 treatment of the standard protocol (Figures S1H). Nevertheless, the frequency of GFP-expressing cells (a surrogate for HDR-mediated gene correction) was reduced in the short protocol (Figure 1I).

Finally, we transplanted GE HSPCs into immunodeficient non-obese diabetic (NOD)-severe combined immunodeficiency (SCID)-$IL2Rg^{-/-}$ (NSG) mice. Thus, we found a significant reduction in the percentage of human $CD45^+$ ($hCD45^+$) engrafted cells in the standard protocol in the peripheral blood (PB), bone marrow (BM), and spleen (SP) (Figures 1J–1L). Analyzing the differentiation output in the PB (Figure S1I), we found an early expansion of myeloid cells and decreased T cells at the last time point in standard protocol conditions (Figure 1M). Conversely, BM and SP graft compositions were comparable within treatments (Figures S1J and S1K). Nonetheless, the percentage of GFP^+ cells was lower in the short protocol editing group (Figures 1N–1P).

Altogether, our results indicate that a longer pre-stimulation heightened the DDR burden and ultimately affected gene-edited HSPC functionality. While minimizing culture time would be favorable for NHEJ-mediated gene disruption, the short protocol is not suitable for HDR-gene correction as it reduced the fraction

(I) Percentage of GFP^+ cells measured by flow cytometry in ATO seeded with HS+AAV6-edited HSPCs ($n = 6$). Wilcoxon test.
(J–L) Percentage of human $CD45^+$ cells in the (J) PB, (K) BM, and (L) SP of mice transplanted with HSPCs edited as indicated ($n = 10, 8, 10, 9$). Mann-Whitney test (calculated at the last time point for PB).
(M) Percentage of B cells, T cells, myeloid, and other cells within the human graft (PB) ($n = 10, 8, 10, 9$). Mann-Whitney test for short vs. standard comparisons.
(N–P) Percentage of GFP^+ cells (within $hCD45^+$) measured in the (N) PB, (O) BM, and (P) SP of mice transplanted with HS+AAV6 HSPCs ($n = 10, 9$). Mann-Whitney test (calculated at the last time point for PB). Mean ± SEM and, unless otherwise specified, lines indicate median values. ns > 0.05; $^*p < 0.05$; $^{**}p < 0.01$; $^{***}p < 0.001$.

of HDR-edited cells, prompting us to investigate HSPC responses to *ex vivo* culture.

HSPC *ex vivo* cell-cycle progression is controlled by the p38 MAPK-ROS axis

As exposure to cytokines and growth factors has been associated with the stress-responsive p38 MAPK,[22–25] we evaluated its activation in HSPCs and found that phospho-p38 MAPK (p-p38) increased upon time in culture across subsets (Figures 2A, S2A, and S2B). Thus, we tested SB203580, a highly specific ATP-competitive inhibitor of p38 MAPK[26] (p38i), treating HSPCs during the first two days of culture (Figure 2B). According to its mechanism of action, p38i suppressed the phosphorylation of MAPKAPK2 (MK2) without impacting HSPC viability (Figures S2C and S2D). Measuring cytosolic ROS and mitochondrial superoxides, we found that HSPCs progressively accumulate oxidative stress, dampened to levels comparable to uncultured HSPCs by p38i administration (Figures 2C, 2D, and S2E). Moreover, mitochondrial respiration analyses revealed lower basal oxygen consumption rate (OCR) and spare respiratory capacity (SRC) upon p38i treatment (Figures 2E, 2F, and S2F). Conversely, measurement of extracellular acidification rate (ECAR) showed slight but consistent higher glycolysis and glycolytic capacity (GC) (Figures 2G, 2H, and S2G), likely implying a metabolic switch toward glycolysis.

As ROS can act as proliferative cues,[27] we reasoned that the primary trigger for adverse HSPC responses to culture may be the sudden onset of p38/ROS-mediated proliferation in otherwise quiescent cells. Thus, we measured the number of cell divisions over seven days of culture across HSPC subsets in vehicle- or p38i-treated cells and employed palbociclib (CDK4/6 inhibitor) as cell-cycle slowdown control. We found that HSPCs performed slightly fewer rounds of cell divisions upon p38i treatment (on average, each cell divided 0.36 times less than control) (Figures 2I and S2H). This effect resulted in an evident reduction in cumulative proliferation, measured by live imaging on bulk HSPCs and, most importantly, on the more HSC-enriched subpopulation (Figures 2J and 2K). To quantitatively assess the duration of cell-cycle phases in single HSPCs, we employed a lentiviral vector encoding for the fluorescent ubiquitination-based cell-cycle indicator 2a system (Fucci2a),[28] which allows discriminating between G1, G1/S transition, and S/G2/M. Comparative analysis revealed a significantly higher median duration of G1/S transition and a slightly longer G1 phase upon p38i (G1/S: 9.05 vs. 5.5 h; G1: 8.75 vs. 6.5 h, respectively); instead, the duration of the HDR-permissive S/G2/M was comparable between conditions (Figure 2L).

To confirm that ROS acts as mitogenic signals in our setting, we employed the ROS scavenger N-acetyl cysteine (NAC). Indeed, NAC supplementation during the first two days of *ex vivo* culture transiently reduced oxidative stress (Figure S2I) and slowed down HSPC proliferation by prolonging all cell-cycle phases (Figures 2M, 2N, and S2J). Nevertheless, NAC treatment did not counteract p38 MAPK activation (Figure S2K). Similarly, additional antioxidants, including resveratrol and tempol, and their combinations with NAC showed a transient ROS reduction (Figure S2L), leading to decreased HSPC proliferation (Figure S2M). However, ROS scavenging was not sufficient to reduce p38 MAPK phosphorylation (Figure S2N), implying that ROS are produced downstream of p38 MAPK activation, as confirmed by similar results obtained by maintaining HSPCs in low-oxygen conditions (hypoxia) (Figure S2O–S2Q).

Our findings highlight that HSPC *ex vivo* culture involves p38 MAPK activation, which controls mitogenic ROS that mediate rapid cell-cycle progression. Notably, p38 inhibition reduces ROS levels and prolongs the G1/S transition duration, slowing down HSPC proliferation alongside mitochondrial respiration and promoting a minor metabolic switch toward glycolysis, a feature associated with slow cycling and more dormant HSCs.[29,30]

p38 MAPK-mediated proliferation stress leads to DNA damage accumulation

Consistent with ROS capacity to oxidize DNA bases, we reported a cumulative 8-oxo-2′-deoxyguanosine (8-oxo-dG) induction, counteracted by p38 inhibition (Figure 3A). Next, we investigated physical single-strand breaks (SSBs) and DSBs accumulation using the alkaline comet assay and found increased DNA damage upon culture, which was mitigated by p38i administration (Figure 3B). Because murine HSCs accumulate DNA damage upon exiting quiescence,[31] we asked whether p38 MAPK-dependent DNA damage would be caused by proliferative stress. Of note, both transient CDK4/6i-mediated cell-cycle inhibition and NAC decreased physical DNA breaks according to the extent of proliferation slowdown, confirming the link between *ex vivo* proliferation and DNA damage accumulation (Figure 3C). We also found increased levels of phosphorylated histone variant H2AX (γH2AX) and phosphorylated replication protein A (pRPA) upon culture, which were rescued by p38 inhibition (Figures 3D, 3E, and S3A). Consistently, p38i alleviated the activation of the apical DNA replication stress kinase ataxia telangiectasia and Rad3-related protein (ATR) (phospho-ATR, Ser428) and its downstream target CHK1 (phospho-CHK1, Ser345) (Figure 3F). Finally, we also reported a slight but persistent increase in the proportion of phenotypically defined primitive HSPCs ($CD34^+133^+90^+$ cells) in the p38i condition (Figure 3G).

Altogether, our data highlight a multi-step process with a precise sequence of events involving p38 MAPK phosphorylation, generation of mitogenic ROS, and alteration of cell-cycle dynamics, leading to consequent proliferation stress and activation of the DDR cascade. Importantly, p38 MAPK inhibition limits the activation of this molecular axis, better preserving primitive HSPCs.

Ex vivo p38 inhibitor administration ameliorates the functionality of gene-edited HSPCs

We reasoned that by decreasing proliferation-associated endogenous DNA damage, p38 inhibition would also mitigate GE-induced detrimental responses and better preserve the long-term functionality of genetically engineered HSPCs. Thus, we cultured HSPCs in the presence of p38i and nucleofected with the HS Cas9 alone or in combination with the GFP-expressing AAV6 (HS+AAV6) required for HDR-mediated GE (Figure 4A). p38i did not affect cell viability nor NHEJ and HDR efficiency across progenitors (Figures S4A–S4C) but preserved the fraction of $CD34^+133^+90^+$ cells and increased HDR-mediated correction

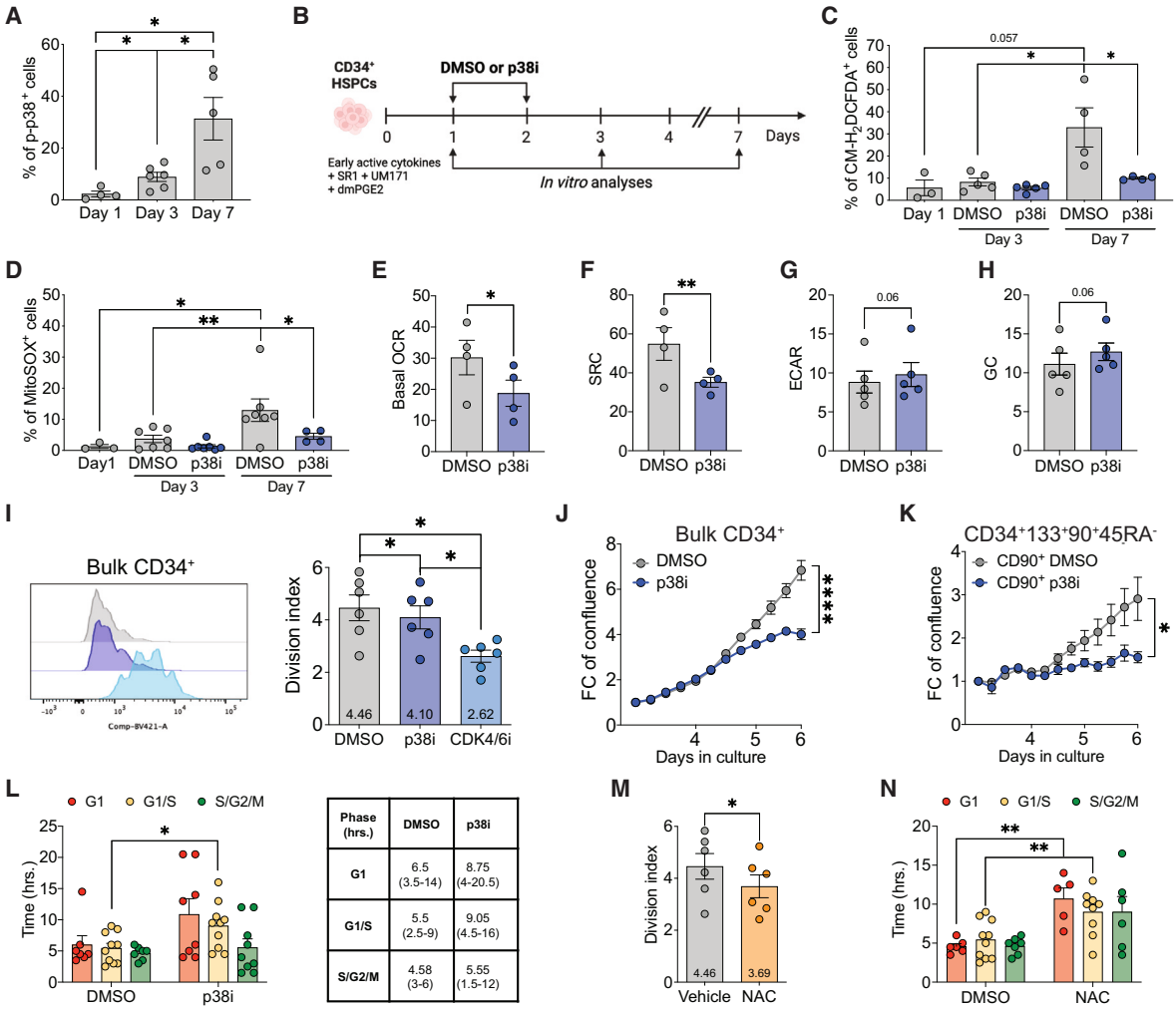

Figure 2. p38 MAPK activation mediates excessive proliferation through mitogenic ROS

(A) Quantification of phospho-p38 by flow cytometry analysis in *ex vivo* cultured HSPCs (n = 4, 6, 5). Mann-Whitney test.

(B) Experimental workflow indicating *in vitro* treatments with DMSO (vehicle) or 4 μM p38i at day 1 and 2 post-thawing of human CB-derived HSPCs. *In vitro* analyses were conducted on days 1, 3, and 7 post-thawing.

(C and D) Quantification of (C) cytosolic ROS detected by CM-H_2DCFDA and of (D) mitochondrial superoxides measured by MitoSOX (C: n = 3, 5, 5, 4, 4; D: n = 3, 7, 7, 7, 4). Mann-Whitney test.

(E and F) Quantification of (E) basal oxygen consumption rate (OCR) or (F) spare respiratory capacity (SRC) after 7 days of culture (n = 4). Mann-Whitney test.

(G and H) Quantification of (G) extracellular acidification rate (ECAR) or (H) glycolytic capacity (GC) after 7 days of culture (n = 5). Wilcoxon test.

(I) Representative plot of CellTrace dilution and division index of $CD34^+$ cells measured at day 7 (n = 6). Wilcoxon test.

(J and K) Cellular confluence of (J) bulk $CD34^+$ or (K) $CD34^+CD133^+CD90^+CD45RA^-$ HSPCs reported as fold change (FC) to the first time point (n = 3). Mann-Whitney test.

(L) Duration (hours) of cell-cycle phases measured in single HSPCs expressing the Fucci2a reporter. Live imaging started on day 2 after p38 inhibitor treatment; each dot represents individual cells. Mann-Whitney test.

(M) Division index of HSPCs measured at day 7 (n = 6). As a control, the DMSO condition from (I) is reported. Wilcoxon test.

(N) Duration (hours) of cell-cycle phases measured in single HSPCs expressing the Fucci2a reporter. Live imaging started on day 2 after NAC treatment; each dot represents individual cells. As a control, the DMSO condition from (L) is reported. Mann-Whitney test. Mean ± SEM. *p < 0.05; **p < 0.01; ****p < 0.0001.

in this primitive subset (Figures 4B, 4C, and S4D). Moreover, p38 inhibition diminished oxidative stress and reduced DNA damage accumulation and ATR/CHK1 activation (Figures 4D–4G), ameliorating GE genotoxicity risk by decreasing MN-bearing HSPCs (Figure 4H). Of note, p38i-treated conditions gave rise to a higher colony number, mostly due to increased mixed-colony output, the progeny of more primitive and multi-potent HSPCs (Figures 4I and 4J). This result was confirmed by secondary colony-forming unit cell (CFU-C) assay, as p38i enhanced the clonogenic output upon serial replating (Figure 4K).

We next assessed the impact of p38 MAPK activity on an adult HSPC source, such as mobilized peripheral blood (mPB). After testing different doses (data not shown), we selected a slightly higher optimal concentration, not affecting cell vitality (Figure S4E),

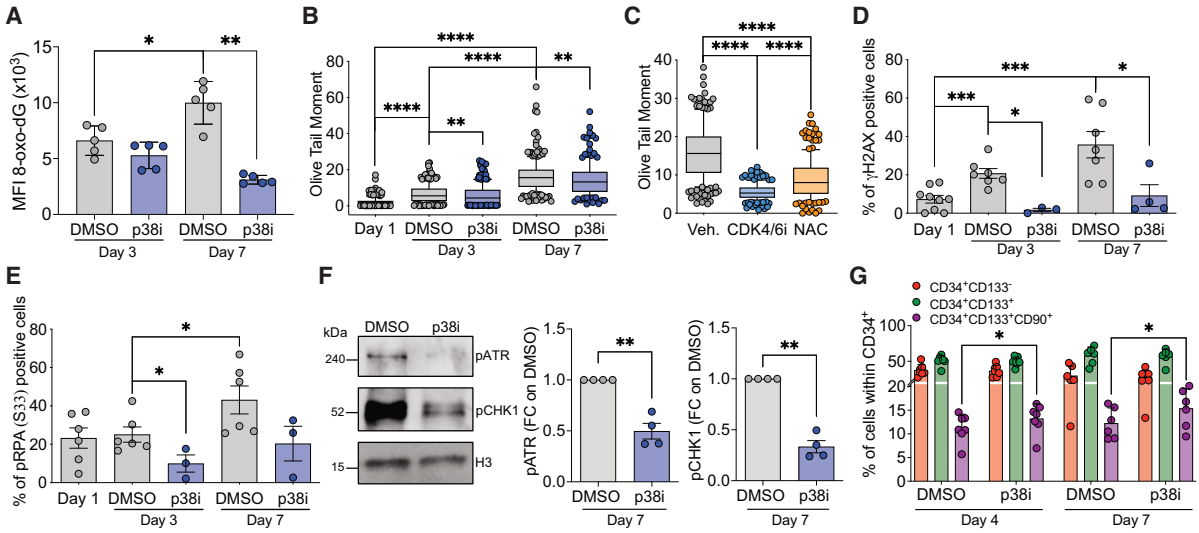

Figure 3. p38 MAPK/ROS triggers proliferation stress and heightens DNA damage

(A) Quantification of 8-oxo-2′-deoxyguanosine by flow cytometry (n = 5). Mann-Whitney test.

(B) Quantification of SSBs and DSBs by comet assay; each point represents a single cell from 3 independent experiments (up to 250 cells were analyzed). Mann-Whitney test. Whiskers represent 10–90 percentile.

(C) Quantification of SSBs and DSBs by comet assay at day 7 of culture; each point represents a single cell from 3 independent experiments (up to 250 cells were analyzed). Mann-Whitney test. Whiskers represent 10–90 percentile.

(D and E) Percentage of (D) γH2AX- or (E) pRPA-positive HSPCs (γH2AX: n = 9, 7, 3, 7, 4; pRPA = n = 6, 6, 3, 6, 3). Mann-Whitney test.

(F) Western blot analysis of pATR (left) and pCHK1 (right) at day 7 (n = 4). Histone H3 was used as a loading control, and fold change relative to control is reported. One-sample t test.

(G) Percentage of HSPC subpopulations ($CD34^+CD133^-$, $CD34^+CD133^+$, and $CD34^+CD133^+CD90^+$ cells) (n = 7). Wilcoxon test. Unless otherwise specified, mean ± SEM. *p < 0.05; **p < 0.01; ***p < 0.001; ****p < 0.0001.

due to increased p38 MAPK activation in mPB $CD34^+$ cells compared to CB (Figure S4F). Nevertheless, p38i treatment in mPB-derived HSPCs did not compromise HDR efficiency and increased the number of mixed colonies (Figures S4G and S4H).

The amelioration of HSPC functionality was specific to p38 signaling blockage, as inhibition of other MAPK, such as c-Jun N-terminal kinase (JNK) and extracellular signal-regulated kinase (ERK),[32,33] slightly promoted cell death, ultimately impairing HSPC *in vitro* clonogenicity (Figures S4I and S4J). Additionally, we also tested whether NAC or low-oxygen conditions could mimic p38i in the GE context. Interestingly, NAC had no impact on ROS accumulation upon GE, which was instead reduced in hypoxia (Figure S4K). Moreover, both conditions showed only a minor effect on HSPC clonogenic potential, slightly decreasing cell viability and lowering HDR correction, especially in the more primitive subset (Figures S4L–S4N), likely due to a more pronounced proliferation slowdown compared to p38 inhibition (Figures 2I, 2M, and S2P).

Overall, p38 inhibition improves gene-corrected HSPC functionality by mitigating proliferation-induced DNA damage that, in addition to GE tools exposure, makes HSPCs exceed a threshold of tolerable DDR and prematurely exhaust.

Single-cell transcriptomics reveals replication stress mitigation and stemness maintenance by p38 inhibition across HSPC subsets

To elucidate p38i-mediated responses across HSPC subsets, we performed droplet-based single-cell RNA sequencing (scRNA-seq). For a more reliable HSC characterization, we enhanced their representation by sorting the HSC-enriched fraction ($CD34^+CD133^+CD90^+CD45RA^-$) and mixed them with the bulk population upon hashtag marking, allowing a comprehensive view of cell composition across not edited, HS Cas9, and HS+AAV6 conditions after vehicle or p38i administration. Moreover, HDR-edited HSPCs were further sorted according to GFP expression (Figure 5A). Through the expression of previously reported marker genes,[35–42] we annotated 15 cell clusters and further validated by computing the module scores of HSC and cell lineage signature from the literature (Figures 5B, S5A, and S5B). Comparison of cluster composition across not edited and HS Cas9 conditions did not reveal major differences upon p38i, while HS+AAV6 samples showed a modest expansion of megakaryocytes-erythroid progenitor (MEP), eosinophil baso-mast progenitor (EBMP)/Baso/Mast, and megakaryocyte erythroid mast cell and basophil progenitor (MEMBP), more evident in the GFP^+ population (Figure 5C; Data S1A). Extrapolating the HSC-sorted fraction, we found an enrichment of cells belonging to the HSC/multi-potent progenitor (MPP) subset, which was slightly more represented upon p38i treatment, especially in the GFP^+ fraction. The same trend was observed for MEP, while MPP was reduced in not edited and GFP^+ cells (Figure 5D; Data S1B). Of note, the higher representation of the HSC/MPP in the GFP^- condition likely reflects their limited propensity to engage HDR.

Gene set enrichment analysis (GSEA) showed significant downregulation of DNA replication, cell cycle, and G2M

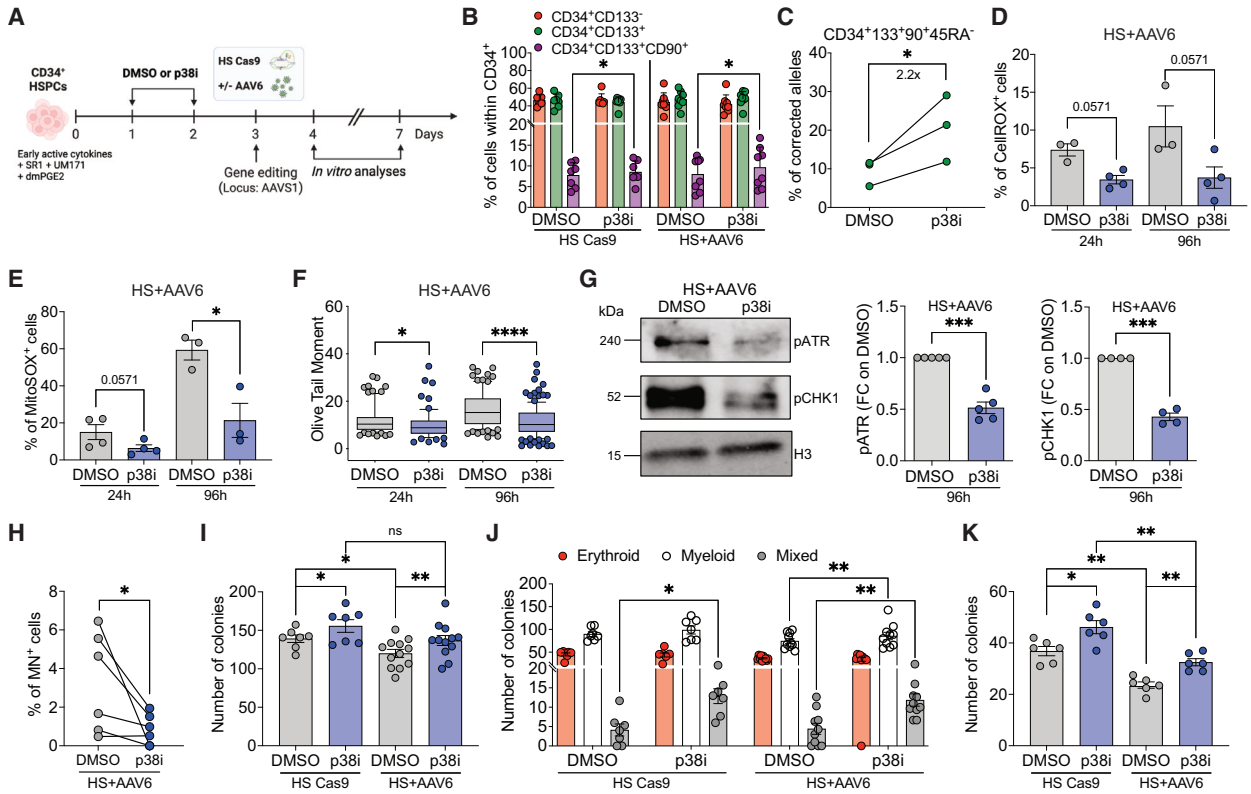

Figure 4. The functionality of gene-edited HSPCs is enhanced by p38 inhibitor treatment

(A) Experimental workflow indicating *in vitro* treatments with vehicle (DMSO) or p38i at day 1 and 2 post-thawing of human CB- or mPB-derived HSPCs. Cells were GE at day 3 by nucleofection of HS Cas9 in the presence or not of AAV6. *In vitro* analyses were conducted on days 4 and 7 (24 and 96 h post-editing, respectively).

(B) Percentage of HSPC subpopulations ($CD34^+CD133^-$, $CD34^+CD133^+$, and $CD34^+CD133^+CD90^+$ cells) at 96 h post-nucleofection (HS Cas9: n = 7, 7, 7; HS+AAV6: n = 8, 8, 8). Wilcoxon test.

(C) Percentage of HDR-corrected alleles at 96 h post-editing in CB-sorted $CD34^+CD133^+CD90^+CD45RA^-$ (n = 3). Mann-Whitney test.

(D and E) Quantification of (D) cytosolic ROS detected by CellROX and of (E) mitochondrial superoxides measured by MitoSOX in HS+AAV6 CB-derived HSPCs (D: n = 3, 4, 3, 4; E: n = 4, 4, 3, 3). Mann-Whitney test.

(F) Quantification of SSBs and DSBs by comet assay in HS+AAV6 CB-derived HSPCs; each point represents a single cell from 2 independent experiments (up to 165 cells were analyzed). Mann-Whitney test. Whiskers represent 10–90 percentile.

(G) Western blot analysis of pATR (left) and pCHK1 (right) at 96 h post-nucleofection in HS+AAV6-edited HSPCs (pATR: n = 5; pCHK1: n = 4). Histone H3 was used as a loading control, and fold change relative to control is reported. One-sample t test.

(H) Percentage of micronuclei-positive HSPCs at 96 h post-editing (HS+AAV6: n = 6). Wilcoxon test.

(I) Number of colonies generated by CB-derived HSPCs plated in methylcellulose 24 h post-treatments (HS Cas9: n = 7; HS+AAV6: n = 12). Wilcoxon test for intra-treatment comparisons or Mann-Whitney test for inter-treatment measurements were performed.

(J) Number of erythroid, myeloid, and mixed colonies from (I). Wilcoxon test.

(K) Number of colonies generated after secondary replating in methylcellulose (n = 6). Mann-Whitney test. Mean ± SEM. ns > 0.05; *p < 0.05; **p < 0.01; ***p < 0.001; ****p < 0.0001.

checkpoint upon p38i, particularly in the HSC/MPP. Instead, hypoxia genes were upregulated across most clusters (Figure 5E), suggesting that p38i may confer a more physiological metabolic phenotype. Similarly, p38i upregulated the PI3K-AKT-mTOR pathway, important to sustain the maintenance of long-term HSCs,[43,44] specifically in the HS+AAV6 condition. Of note, gene lists of G1/S transition and cell-cycle regulation analyses confirmed and extended our molecular data on HSPC proliferation kinetics to GE cells (Figure 5E; Data S1C). Interestingly, RNA processing and translation showed a different behavior among conditions with upregulation in not edited and HS Cas9-treated cells and an opposite orientation in HS+AAV6 GFP^- and GFP^+ samples, likely reflecting a distinctive response to p38i in cells exposed to the AAV6 vector (Figure 5E). Cell-cycle inferences revealed a marked S phase representation in not edited cells, even for the HSC/MPP cluster, which was reduced in HS Cas9 and HS/AAV6 conditions. Consistently, p38i enriched G1 representation in all conditions across most clusters, including the HSC/MPP cluster (Figures 5F and S5C; Data S1D and S1E).

Furthermore, we assessed possible changes in HSC/MPP replication dynamics and found downregulation of replication

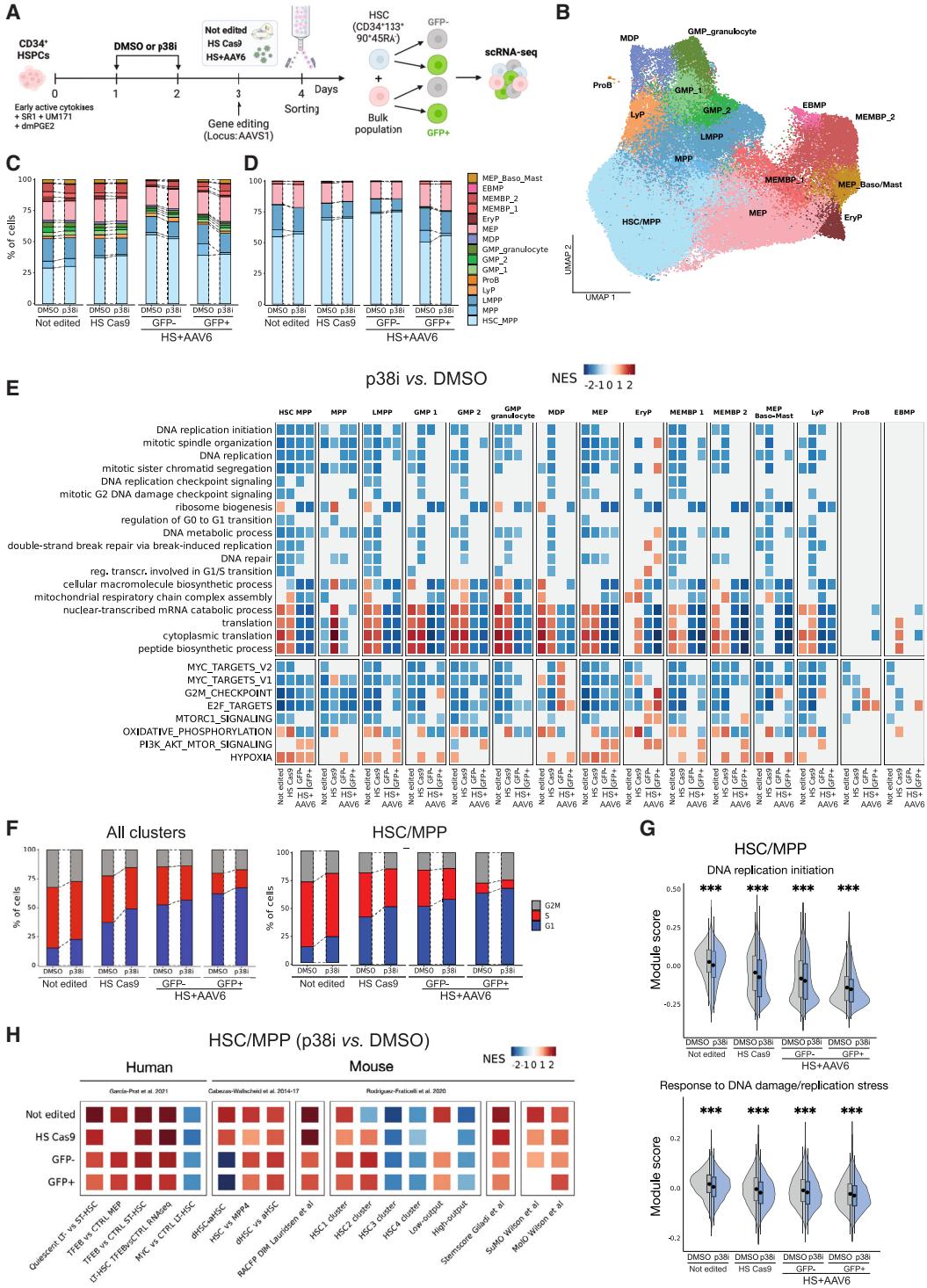

Figure 5. Single-cell transcriptomic analysis reveals replication stress mitigation and stemness maintenance by p38 inhibition across conditions

(A) Schematic representation of the single-cell RNA transcriptomic analysis experimental workflow: at day 1 and 2 post-thawing human CB-derived HSPCs were treated with vehicle (DMSO) or p38i. At day 3, cells were nucleofected with HS Cas9 in the presence or not of AAV6. A not edited control was included. At day 4 (24 h post-editing), HSPCs were sorted and collected for subsequent analyses.

(B) Uniform manifold approximation and projection (UMAP) of annotated populations with cells belonging to all conditions.

(C and D) Barplots showing the distribution of (C) all the cells retrieved and (D) $CD34^{+}CD133^{+}CD90^{+}CD45RA^{-}$ assigned to each subpopulation.

(legend continued on next page)

initiation and response to DNA damage and replication stress programs[34] upon p38i, further supporting that proliferation slowdown mitigates culture-triggered DNA damage (Figure 5G). We also found modest downregulation of genes involved in DNA replication fork restart (*WRN, DNA2*) and repriming (*PRIMPOL*, *BLM*), likely resulting in reduced discontinuous DNA synthesis and single-stranded DNA gap accumulation. Similarly, we found in not edited and HS Cas9 p38i-treated cells reduced expression of genes involved in fork reversal, which were conversely upregulated in the HS+AAV6 condition, suggesting that HSPCs may be more prone to activate this DNA repair pathway in response to viral sensing (Figure S5D). Lastly, p38 inhibition increased HSC/MPP cells harboring molecular signatures of self-renewal, dormancy, metabolic fitness, and higher repopulating capacity[29,45–49] (Figure 5H).

Collectively, these data link p38 MAPK-mediated DNA replication control with reduced fitness in unmanipulated and genetically engineered HSCs, as putatively identified in our single-cell analysis, that could be mitigated by p38 inhibition.

Multi-lineage differentiation of primitive HDR-corrected HSCs is enhanced by p38 inhibition

To simultaneously address the impact of culture and genetic engineering on HSC lineage specification, we fluorescence-activated cell sorting (FACS) sorted the HSC-enriched fraction post-thawing, post-culture, and GE (Figures 6A and S6A) and characterized the differentiation potential along the myeloid (My), lymphoid (Ly), megakaryocytes (Meg), and erythroid (Ery) lineages[50] (Figure S6B). First, we reported that culture *per se* increases the fraction of cells incapable of differentiating and uni-lineage colonies at the expense of multi-lineage potential. This effect was further exacerbated by GE, especially in the fraction of cells that had undergone HDR (GFP^+) compared to cells that did not integrate the GFP cassette (GFP^-), although they had likely experienced AAV6 exposure and repaired nuclease-induced DSB by NHEJ (Figure 6B). Accordingly, also the cellularity of colonies was reduced upon culture and in response to GE in the fraction of HDR-corrected cells (Figure 6C). Next, we assessed how p38 MAPK inhibition impacts HSC multi-potency (Figure 6A). While p38i did not rescue the impact of GE on HSC clonogenic capacity (Figure S6C), both not edited and HS+AAV6 p38i-treated cells generated more multi-lineage colonies (Figure 6D). By analyzing the composition of uni-lineage and multi-lineage colonies (Figure S6D), we reported fewer My-only and Ery-only colonies upon p38i (Figure S6E). Instead, among multi-lineage colonies, p38 inhibition expanded My/Ery and My/Ery/Meg colonies in not edited (NE) conditions, and My/Meg, Ery/Meg, My/Ery/Meg, My/natural killer (NK)/Ery, and even of the rarest NK/Ery/Meg, My/NK/Meg, and My/NK/Ery/Meg colonies in GE HSCs (Figure 6E).

We next evaluated HSC multi-potency specifically in HDR-edited cells and found that despite there being no differences in the clonogenic efficiency (Figure S6F), we detected a higher percentage of multi-lineage colonies from both GFP^- and GFP^+ HSCs when pre-treated with p38i (Figures 6F and S6G). Indeed, we observed fewer My-only and Ery-only colonies (Figure S6H), while the composition of some multi-lineage colonies was sample specific and treatment independent: in particular, NK/Meg and My/NK/Ery colonies derived only from GFP^+ HSCs, which also showed an expansion of My/NK colonies compared to GFP^-. Among treatment-driven changes, p38i expanded My/Meg, Ery/Meg, My/Ery/Meg, and other tri- and quadri-lineage colonies in GFP^- and/or GFP^+ HSCs (Figure 6G).

Altogether, these data indicate that *ex vivo* culture and GE affect HSC differentiation at the single-cell level that can be rescued by p38 inhibition, ameliorating multi-lineage differentiation and enhancing erythroid and megakaryocyte stem-proximal outputs.

p38 MAPK inhibition improves gene-edited HSPC repopulating capacity and clonal output long-term post-transplantation

To test the impact of p38 inhibition before GE on reconstitution capacity, we transplanted HSPCs nucleofected with the HS Cas9 or HS+AAV6 upon treatment into NSG mice. After 15 weeks, $CD34^+$ HSPCs were purified from the mice and re-challenged in clonogenic assay or injected into secondary recipients (Figure 7A). By measuring human chimerism in PB, BM, and SP, we found that while the engraftment of the HS Cas9 groups was similar, likely due to saturation of the host, the engraftment of p38i-treated HS+AAV6 HSPCs was significantly higher than that of control (Figures 7B, 7C, and S7A). In addition, we found an early reduction of myeloid cells in HS+AAV6 and more T cells at the last time point in HS Cas9 of the p38i condition (Figure S7B). While similar results were reported in the SP, BM graft compositions were comparable between treatments (Figure S7C and S7D). Additionally, the percentage of GFP-expressing cells was similar across organs and conditions (Figures 7D, 7E, and S7E). Nonetheless, p38i increased the overall yield of gene-corrected cells due to the higher engraftment. Upon $CD34^+$ cell retrieval from the BM of the mice, we reported a higher colony output in the p38i-treated conditions (Figures 7F and 7G).

Because we recently demonstrated that GE affects the clonal repertoire of edited HSPCs,[11] we asked whether p38 inhibition could impact the number of reconstituting edited clones. Indeed, we reported improved clonal diversity in both p38i conditions when measuring NHEJ-induced insertion or deletion (indel) diversity (Figure 7H). To determine HDR-clonal output, we used an AAV6 carrying a "barcode" sequence (BAR)[11] and found enhanced polyclonal reconstitution of HDR-edited clones upon p38 inhibition (Figure 7I). Moreover, inter-mouse BAR sharing

(E) Enriched terms obtained performing GSEA of intra-condition comparisons of p38i vs. vehicle. Rows report terms enriched in at least one of the comparisons (columns) (false discovery rate < 0.1) from the gene ontology (GO), biological processes (BP), and the hallmark signatures (MSigDB). Colors indicate negative/positive normalized enrichment score (NES).

(F) Percentage of cell-cycle distribution across all the cell subpopulations (left) or the HSC cluster (right).

(G) Module score of DNA replication initiation and response to DNA damage/replication stress signatures as in Jacobs et al.[34] Wilcoxon test (***$p < 0.001$).

(H) GSEA analysis of intra-condition comparisons of p38i vs. vehicle of HSPC-related categories retrieved from the literature (see STAR Methods).

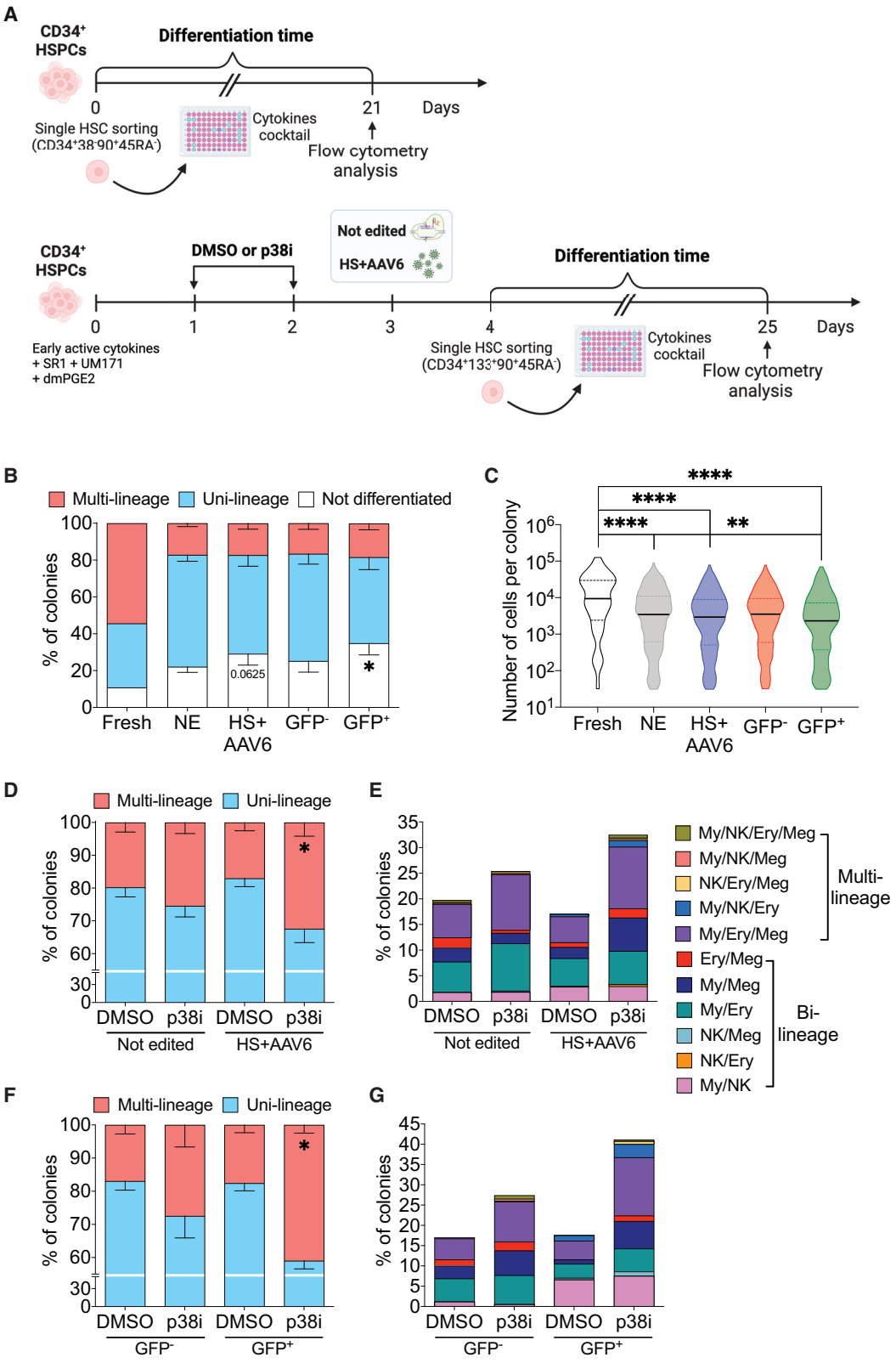

(legend on next page)

revealed few pre-infusion duplications of HDR-edited HSPCs that maintained repopulation potential upon transplantation[11] (Figure S7F).

These findings were recapitulated by transplanting in NSG mice mPB-derived CD34$^+$ cells (HS+AAV6). Indeed, p38i increased human engraftment without compromising the percentage of HDR-corrected cells in PB and BM (Figures S7G–S7J) and enhanced the clonogenic potential with mixed-colony expansion from BM-derived CD34$^+$ cells (Figures S7K and S7L).

Finally, to specifically test the repopulating capacity of long-term HSCs, we injected BM-derived CD34$^+$ cells into secondary recipients (Figure 7J). Thus, we reported higher human chimerism in the p38i group in PB and SP (Figures 7K and S7M), while similar engraftment was found in the BM (Figure 7L). Strikingly, only the p38i group retained a sizable fraction of HDR-edited cells (Figures 7M, 7N, and S7N). In addition, when analyzing the impact of p38i on graft composition, we found that the p38i-treated group showed fewer myeloid cells at early and late time points post-transplant and more T cells at the endpoint (Figures 7O, S7O, and S7P).

Overall, our data indicate that p38i treatment prior to GE improves polyclonal reconstitution of HDR-edited HSCs and better preserves their long-term repopulating capacity through serial transplantation.

DISCUSSION

HSPC *ex vivo* culture is required for HDR engagement in long-range gene correction for clinical applications. Here, we reported that *ex vivo* culture contributes to GE HSC functional impairment and investigated the mechanism behind such dysfunction. Through a side-by-side comparison between a short (overnight activation) and a standard protocol (three days of pre-stimulation), we found that the p53-mediated DDR activation, triggered by concomitant exposure to CRISPR-Cas9-induced DSBs and AAV6 vectors,[12] was higher and more prolonged in HSPCs subjected to the standard protocol, resulting in decreased colony number and impaired repopulating capacity, with higher myeloid skewing and lower T cell differentiation, resembling the output of aged HSCs.[51–53] While these effects were mitigated in the short protocol, HDR efficiency was drastically lower and insufficient to guarantee an optimal representation of gene-corrected cells upon transplant. For these reasons, shortening pre-stimulation time should be envisioned specifically for gene disruption by NHEJ.

To identify dysfunction determinants during *ex vivo* culture, we uncovered a molecular axis that links p38 MAPK activation, ROS, and proliferation stress to loss of multi-potency and reduced repopulating capacity of genetically engineered HSPCs. Distinctively from previous works,[14,15,18,54] we showed that p38 MAPK triggers ROS that are primarily mitogenic and fuel faster proliferation, as demonstrated by the alteration of cell-cycle dynamics upon antioxidant administration and low-oxygen conditions. Consequently, excessive proliferation mediates the accumulation of DNA damage with markers of DNA replication stress, including activation of the ATR-CHK1 DDR axis. Even if we cannot completely rule out p38 MAPK involvement in other aspects of culture adaptation,[55] our study shows that longer G1 phase and G1/S transition are associated with reduced DNA damage and DDR levels after *ex vivo* culture, likely by limiting replication forks stalling as suggested in murine embryonic stem cells.[56] While most efforts in the GE field have focused on promoting cell-cycle progression and/or favoring HDR,[7,11] our work highlights that faster proliferation may initiate premature exhaustion of engineered HSPCs. Similarly, slowing cell-cycle progression should be considered in *ex vivo* expansion protocols,[44,57,58] which are particularly relevant for genetic diseases with limited BM harvest or HSPC mobilization.[59]

Although we detected a similar percentage of GFP$^+$ cells in primary recipients, only the p38i group retained a sizable fraction of long-term HDR-corrected HSCs in secondary transplantation. Deep sequencing revealed a more polyclonal graft in edited HSPCs upon p38i treatment in clones that underwent NHEJ and HDR. This gain in the clonal repertoire is particularly relevant for clinical translation as an oligoclonal graft might delay hematopoietic recovery after conditioning, restricting the presence of corrected HSPCs in the long term and favoring the emergence of clonal hematopoiesis, possibly affecting the overall safety of the procedure.[11] Moreover, both shortening time in culture and p38i treatment diminished the percentage of MNs-positive HSPCs, and although their fate upon the replicative stress imposed by transplantation remains unknown, our data suggest that p38i will likely endow engineered HSPCs with improved safety profile.

In conclusion, our study sheds light on the mechanisms contributing to the functional impairment of genetically engineered HSPCs by providing molecular details on how human HSPCs cope with endogenous stress during *ex vivo* culture. Our data uncover the p38 MAPK-ROS axis as a key regulator of cell-cycle progression and heightened DNA damage in engineered HSPCs and highlights a strategy based on temporary inhibition of p38 MAPK prior to genetic manipulation to endow edited HSCs with superior long-term and polyclonal repopulating capacity for wider and safer GT applications.

Figure 6. *In vitro* multi-potency of GE HSCs is enhanced by p38 MAPK inhibition

(A) Experimental workflow of the single-cell differentiation assay. CB-derived HSPCs were FACS-sorted and seeded as single cells in a cytokine-enriched medium immediately after thawing (fresh), or at day 4 for not edited and HS+AVV6 conditions. Colonies were harvested and analyzed after 25 days of culture.
(B) Percentage of not differentiated, uni-lineage, and multi-lineage colonies. HS+AAV6 condition was subsequently analyzed as GFP$^-$ and GFP$^+$ colonies. >100 colonies for fresh condition and >1,000 colonies for all the other conditions from 4 independent experiments were analyzed. Mann-Whitney test.
(C) Distribution of the number of cells composing individual colonies analyzed in (B). Mann-Whitney test.
(D) Percentage of uni-lineage and multi-lineage colonies. >1,000 colonies analyzed from 4 independent experiments. Mann-Whitney test.
(E) Percentage of colonies with the indicated composition derived from multi-lineage colonies in (D).
(F) Percentage of uni-lineage and multi-lineage colonies derived from HS+AAV6 in (D). Mann-Whitney test.
(G) Percentage of colonies with the indicated composition derived from multi-lineage colonies in (F). Mean ± SEM. *$p < 0.05$; **$p < 0.01$; ****$p < 0.0001$.

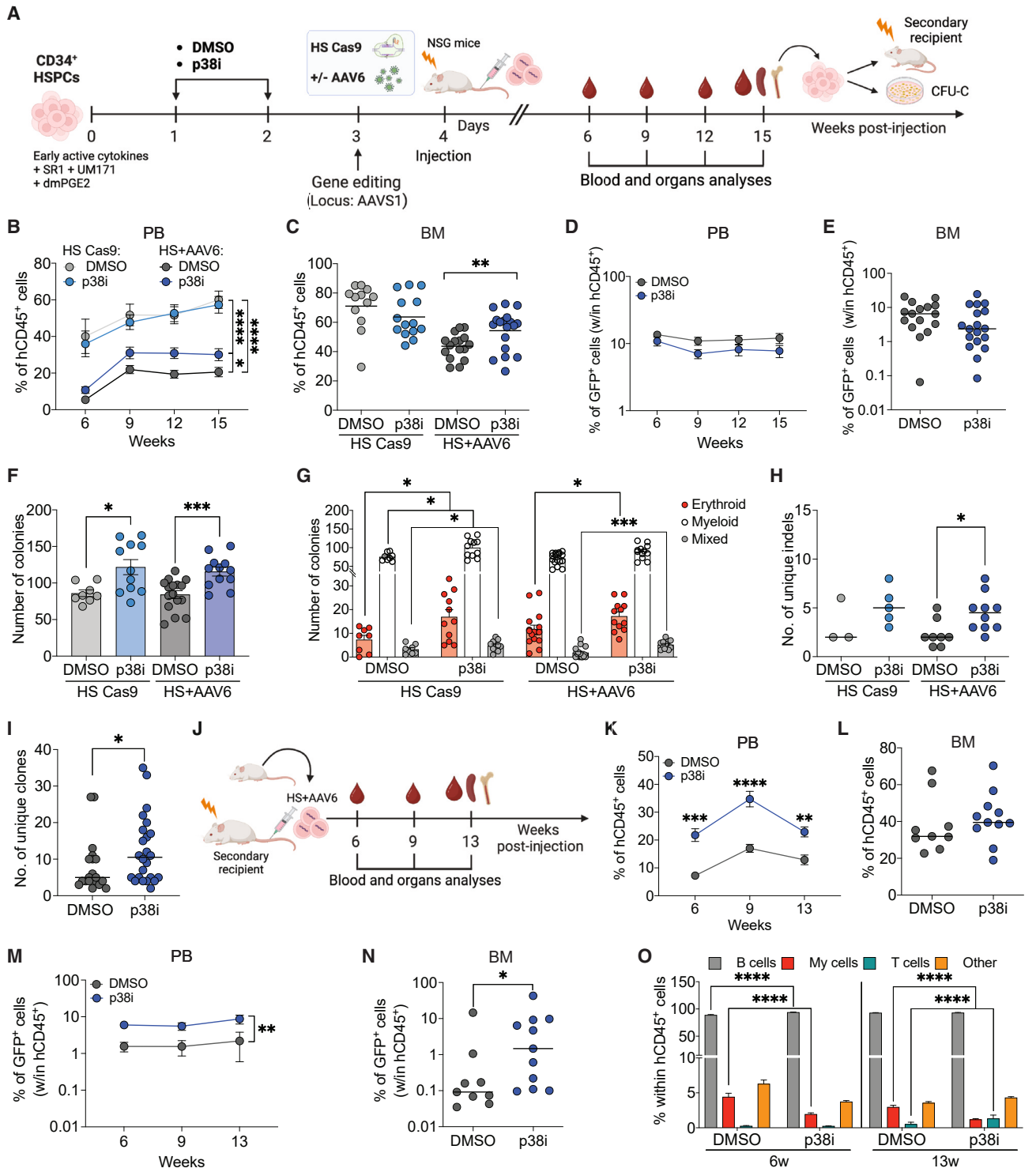

Figure 7. Repopulating capacity and clonal repertoire of GE HSPCs are ameliorated by p38 inhibitor administration

(A) Experimental workflow showing the time of *in vitro* treatments, GE, and *in vivo* injection of human CB- or mPB-derived HSPCs into NSG mice, followed by blood and organ analyses.

(B and C) Percentage of human CD45$^+$ cells in the (B) PB and (C) BM of NSG mice transplanted with CB-derived HSPCs edited as indicated (n = 12, 14, 16, 18). Mann-Whitney test (calculated at the last time point for PB).

(D and E) Percentage of GFP$^+$ cells (within hCD45$^+$ cells) in the (D) PB and (E) BM of mice from (B and C) (n = 16, 18). Mann-Whitney test.

(legend continued on next page)

Limitations of the study

Our study utilized HSPCs from healthy donors, which may not fully reflect the behavior of patient-derived cells. To gain more clinically relevant insights, similar experiments should be conducted on HSPCs from patients with disease-specific backgrounds. Although we observed improved engraftment, clonal output, and persistence of HDR-edited HSCs in xenotransplant models, clinical trials are needed to confirm the therapeutic benefits of p38 inhibition in GE approaches. Finally, while we consistently observed reduced DNA damage and MN accumulation in HSPCs edited in the presence of p38 inhibitor, further investigation into potential genotoxic effects is required before clinical application.

RESOURCE AVAILABILITY

Lead contact

The lead contact for this work is Raffaella Di Micco (dimicco.raffaella@hsr.it).

Materials availability

This study did not generate new reagents.

Data and code availability

- scRNA-seq data have been deposited in the NCBI's Gene Expression Omnibus (GEO: GSE238189) and are publicly available.
- The code used for the analysis is available at the following GitLab repository: http://www.bioinfotiget.it/gitlab/custom/dellavolpe_geneediting/dellavolpe_scrna-seq.
- Any additional raw data and information required to reanalyze the data reported in this paper are available from the lead contact upon request.

ACKNOWLEDGMENTS

We thank A. Jacob for technical help with BAR-seq library preparation, R. De Marco for micronuclei quantification, the FRACTAL and ALEMBIC facilities at San Raffaele Hospital, and the biostatisticians at Centro Universitario di Statistica per le Scienze Biomediche (CUSSB) for advice on statistical analyses. L.d.V., R.V., F.M., and D.G. conducted this study partially fulfilling their Ph.D. in Molecular Medicine, Vita-Salute San Raffaele University, Milan, Italy. G.F. conducted this study partially fulfilling his Ph.D. in Translational and Molecular Medicine – DIMET University of Milano Bicocca. L.d.V. was funded by Assegno di Ricerca Fronzaroli. A.C. is an early career scientist in the EHA and ASH TRTH. T.T. is enrolled in the EHA-EMBL/EBI computational biology training in hematology. A.S. is funded by EMBO long-term postdoctoral fellowship (awarded ALTF-245-2022). Work in the R.D.M., L.N., and B.G. lab was supported by a Horizon Europe 2020 Program X-PAND grant (G.A. 101070950). The R.D.M. laboratory was supported by a Career Development award from the Human Frontier Science Program, the New York Stem Cell Foundation, a My First AIRC grant (MFAG 2019–PI ID.23321), the European Research Council (consolidator grant 101003186, ReviveSTEM), and Fondazione Telethon (SR-Tiget Core Grant, Tele21-E5). R.D.M. is a New York Stem Cell Foundation Robertson Investigator.

AUTHOR CONTRIBUTIONS

L.d.V., F.M., and R.V. planned and performed experiments and analyzed and interpreted the data; L.A. contributed to various *in vitro* experiments; T.T. and M.B. performed bioinformatics analysis and interpreted computational data; S.B. performed clonal tracking analyses; I.M. coordinated the bioinformatics analysis; M.M.N. and B.G. provided intellectual input for scRNA-seq experimental design and analysis; C.B. and S.P. performed ATO experiments; G.F. performed seahorse experiments; E.L.F. performed WB experiments; S.F. and A. Varesi helped with library preparations for clonal tracking analysis. A. Villa supervised C.B. and S.P. and critically discussed the manuscript; S.F. and L.N. supervised A. Varesi and critically discussed the manuscript; A.S. helped with single-cell differentiation experiments; D.G., A.C., K.G., and E.C. provided technical help for animal experiments; K.G. helped with molecular assays and provided intellectual input and critical discussion. R.D.M. designed, coordinated, and interpreted the data, secured funding, and supervised the research. L.d.V., F.M., and R.D.M. wrote the manuscript with input from all the authors.

DECLARATION OF INTERESTS

R.D.M., L.d.V., F.M., A.C., L.N., and S.F. are inventors of patents on applications of gene editing in HSPCs owned and managed by the San Raffaele Scientific Institute and the Telethon Foundation. L.N. is a founder and quota holder of GeneSpire.

STAR★METHODS

Detailed methods are provided in the online version of this paper and include the following:

- KEY RESOURCES TABLE
- EXPERIMENTAL MODEL AND STUDY PARTICIPANT DETAILS
  - Mice
  - Primary cell cultures
- METHOD DETAILS
  - *In vitro* treatments
  - Gene editing
  - Colony-forming unit cell assay
  - Artificial thymic organoid (ATO) system
  - Single-cell differentiation assay
  - CD34$^+$ HSPC xenotransplantation studies in NSG mice
  - NHEJ analysis
  - Digital droplet PCR (ddPCR)
  - Quantitative PCR (qPCR)
  - Flow cytometry
  - Immunofluorescence analysis
  - Comet assay
  - Seahorse metabolic flux analysis
  - Western blot
  - EdU incorporation and detection for flow cytometry
  - Live imaging analysis of confluency
  - Cell trace violet
  - Cell cycle analyses with the Fucci2a system
  - BAR- and indels-based clonal tracking libraries

(F) Number of colonies formed by BM-derived CD34$^+$ cells purified from mice in (C) (HS Cas9: n = 8, 11; HS + AAV6: n = 16, 12). Mann-Whitney test.
(G) Number of erythroid, myeloid, and mixed colonies from samples in (F). Mann-Whitney test.
(H) Number of unique indels in human BM-derived cells (HS Cas9: n = 3, 5; HS+AAV6: n = 8, 10). Median values are reported. Mann-Whitney test.
(I) Number of unique BARs in HS+AAV6 human BM-derived cells (n = 19, 24). Median values are reported. Mann-Whitney test.
(J) Schematic representation of the secondary transplantation: BM-derived CD34$^+$ cells recovered from primary mice were injected into secondary recipients. Hematopoietic organs were analyzed at the endpoint (13 weeks).
(K and L) Percentage of hCD45$^+$ cells in the (K) PB and (L) BM of secondary-transplanted mice (n = 9, 11). Mann-Whitney test.
(M and N) Percentage of GFP$^+$ cells (within hCD45$^+$ cells) in the (M) PB and (N) BM of mice in (K and L) (n = 9, 11). Mann-Whitney tests.
(O) Percentage of B cells, T cells, myeloid, and other cells within hCD45$^+$ cells in the PB of mice in (K) (n = 9, 11). Mann-Whitney test. Mean ± SEM and, unless otherwise specified, lines indicate median values. *p < 0.05; **p < 0.01; ***p < 0.001; ****p < 0.0001.

- BAR-seq analysis
- Indels-based clonal tracking analysis
- Single-cell RNA-sequencing and analysis

- QUANTIFICATION AND STATISTICAL ANALYSIS

SUPPLEMENTAL INFORMATION

Supplemental information can be found online at https://doi.org/10.1016/j.xcrm.2024.101823.

Received: March 22, 2024
Revised: August 26, 2024
Accepted: October 18, 2024
Published: November 12, 2024

REFERENCES

1. Naldini, L., Cicalese, M.P., Bernardo, M.E., Gentner, B., Gabaldo, M., Ferrari, G., and Aiuti, A. (2022). The EHA Research Roadmap: Hematopoietic Stem Cell Gene Therapy. HemaSphere *6*, E671.
2. Ferrari, S., Valeri, E., Conti, A., Scala, S., Aprile, A., Di Micco, R., Kajaste-Rudnitski, A., Montini, E., Ferrari, G., Aiuti, A., and Naldini, L. (2023). Genetic engineering meets hematopoietic stem cell biology for next-generation gene therapy. Cell Stem Cell *30*, 549–570.
3. Doudna, J.A., and Charpentier, E. (2014). The new frontier of genome engineering with CRISPR-Cas9. Science *346*, 1258096.
4. Porteus, M.H. (2019). A New Class of Medicines through DNA Editing. N. Engl. J. Med. *380*, 947–959.
5. Scully, R., Panday, A., Elango, R., and Willis, N.A. (2019). DNA double-strand break repair-pathway choice in somatic mammalian cells. Nat. Rev. Mol. Cell Biol. *20*, 698–714.
6. Symington, L.S. (2014). End resection at double-strand breaks: Mechanism and regulation. Cold Spring Harb. Perspect. Biol. *6*, a016436.
7. Lomova, A., Clark, D.N., Campo-Fernandez, B., Flores-Bjurström, C., Kaufman, M.L., Fitz-Gibbon, S., Wang, X., Miyahira, E.Y., Brown, D., DeWitt, M.A., et al. (2019). Improving Gene Editing Outcomes in Human Hematopoietic Stem and Progenitor Cells by Temporal Control of DNA Repair. Stem Cell. *37*, 284–294.
8. Genovese, P., Schiroli, G., Escobar, G., Tomaso, T.D., Firrito, C., Calabria, A., Moi, D., Mazzieri, R., Bonini, C., Holmes, M.C., et al. (2014). Targeted genome editing in human repopulating haematopoietic stem cells. Nature *510*, 235–240.
9. Rai, R., Romito, M., Rivers, E., Turchiano, G., Blattner, G., Vetharoy, W., Ladon, D., Andrieux, G., Zhang, F., Zinicola, M., et al. (2020). Targeted gene correction of human hematopoietic stem cells for the treatment of Wiskott - Aldrich Syndrome. Nat. Commun. *11*, 4034.
10. De Ravin, S.S., Brault, J., Meis, R.J., Liu, S., Li, L., Pavel-Dinu, M., Lazzarotto, C.R., Liu, T., Koontz, S.M., Choi, U., et al. (2021). Enhanced homology-directed repair for highly efficient gene editing in hematopoietic stem/progenitor cells. Blood *137*, 2598–2608.
11. Ferrari, S., Jacob, A., Beretta, S., Unali, G., Albano, L., Vavassori, V., Cittaro, D., Lazarevic, D., Brombin, C., Cugnata, F., et al. (2020). Efficient gene editing of human long-term hematopoietic stem cells validated by clonal tracking. Nat. Biotechnol. *38*, 1298–1308.
12. Schiroli, G., Conti, A., Ferrari, S., Della Volpe, L., Jacob, A., Albano, L., Beretta, S., Calabria, A., Vavassori, V., Gasparini, P., et al. (2019). Precise Gene Editing Preserves Hematopoietic Stem Cell Function following Transient p53-Mediated DNA Damage Response. Cell Stem Cell *24*, 551–565.e8.
13. Conti, A., and Di Micco, R. (2018). p53 activation: A checkpoint for precision genome editing? Genome Med. *10*, 66.
14. Jang, Y.Y., and Sharkis, S.J. (2007). A low level of reactive oxygen species selects for primitive hematopoietic stem cells that may reside in the low-oxygenic niche. Blood *110*, 3056–3063.
15. Tesio, M., Tang, Y., Müdder, K., Saini, M., von Paleske, L., Macintyre, E., Pasparakis, M., Waisman, A., and Trumpp, A. (2015). Hematopoietic stem cell quiescence and function are controlled by the CYLD-TRAF2-p38MAPK pathway. J. Exp. Med. *212*, 525–538.
16. Henry, E., Souissi-Sahraoui, I., Deynoux, M., Lefèvre, A., Barroca, V., Campalans, A., Ménard, V., Calvo, J., Pflumio, F., and Arcangeli, M.L. (2020). Human hematopoietic stem/progenitor cells display reactive oxygen species-dependent long-term hematopoietic defects after exposure to low doses of ionizing radiations. Haematologica *105*, 2044–2055.
17. Zou, J., Zou, P., Wang, J., Li, L., Wang, Y., Zhou, D., and Liu, L. (2012). Inhibition of p38 MAPK activity promotes ex vivo expansion of human cord blood hematopoietic stem cells. Ann. Hematol. *91*, 813–823.
18. Li, X., Ma, X., Chen, Y., Peng, D., Wang, H., Chen, S., Xiao, Y., Li, L., Zhou, H., Cheng, F., et al. (2020). Coinhibition of activated p38 MAPKα and mTORC1 potentiates stemness maintenance of HSCs from SR1-expanded human cord blood $CD34^+$ cells via inhibition of senescence. Stem Cells Transl. Med. *9*, 1604–1616.
19. Hendel, A., Bak, R.O., Clark, J.T., Kennedy, A.B., Ryan, D.E., Roy, S., Steinfeld, I., Lunstad, B.D., Kaiser, R.J., Wilkens, A.B., et al. (2015). Chemically modified guide RNAs enhance CRISPR-Cas genome editing in human primary cells. Nat. Biotechnol. *33*, 985–989.
20. Leibowitz, M.L., Papathanasiou, S., Doerfler, P.A., Blaine, L.J., Sun, L., Yao, Y., Zhang, C.Z., Weiss, M.J., and Pellman, D. (2021). Chromothripsis as an on-target consequence of CRISPR–Cas9 genome editing. Nat. Genet. *53*, 895–905.
21. Castiello, M.C., Brandas, C., Ferrari, S., Porcellini, S., Sacchetti, N., Canarutto, D., Draghici, E., Merelli, I., Barcella, M., Pelosi, G., et al. (2024). Exonic knockout and knockin gene editing in hematopoietic stem and progenitor cells rescues RAG1 immunodeficiency. Sci. Transl. Med. *16*, eadh8162.
22. Desterke, C., Bilhou-Nabéra, C., Guerton, B., Martinaud, C., Tonetti, C., Clay, D., Guglielmelli, P., Vannucchi, A., Bordessoule, D., Hasselbalch, H., et al. (2011). FLT3-mediated p38-MAPK activation participates in the control of megakaryopoiesis in primary myelofibrosis. Cancer Res. *71*, 2901–2915.
23. Ezumi, Y., Nishida, E., Uchiyama, T., and Takayama, H. (1999). Thrombopoietin potentiates agonist-stimulated activation of p38 mitogen-activated protein kinase in human platelets. Biochem. Biophys. Res. Commun. *261*, 58–63.
24. Nishikai-Yan Shen, T., Kanazawa, S., Kado, M., Okada, K., Luo, L., Hayashi, A., Mizuno, H., and Tanaka, R. (2017). Interleukin-6 stimulates Akt and p38 MAPK phosphorylation and fibroblast migration in non-diabetic but not diabetic mice. PLoS One *12*, e0178232.
25. Sundström, M., Alfredsson, J., Olsson, N., and Nilsson, G. (2001). Stem cell factor-induced migration of mast cells requires p38 mitogen-activated protein kinase activity. Exp. Cell Res. *267*, 144–151.
26. Cuenda, A., Rouse, J., Doza, Y.N., Meier, R., Cohen, P., Gallagher, T.F., Young, P.R., and Lee, J.C. (1995). SB 203580 is a specific inhibitor of a MAP kinase homologue which is stimulated by cellular stresses and interleukin-1. FEBS Lett. *364*, 229–233.
27. Ogrunc, M., Di Micco, R., Liontos, M., Bombardelli, L., Mione, M., Fumagalli, M., Gorgoulis, V.G., and d'Adda di Fagagna, F. (2014). Oncogene-induced reactive oxygen species fuel hyperproliferation and DNA damage response activation. Cell Death Differ. *21*, 998–1012.
28. Pineda, G., Lennon, K.M., Delos Santos, N.P., Lambert-Fliszar, F., Riso, G.L., Lazzari, E., Marra, M.A., Morris, S., Sakaue-Sawano, A., Miyawaki, A., and Jamieson, C.H.M. (2016). Tracking of Normal and Malignant Progenitor Cell Cycle Transit in a Defined Niche. Sci. Rep. *6*, 23885.
29. García-Prat, L., Kaufmann, K.B., Schneiter, F., Voisin, V., Murison, A., Chen, J., Chan-Seng-Yue, M., Gan, O.I., McLeod, J.L., Smith, S.A., et al. (2021). TFEB-mediated endolysosomal activity controls human hematopoietic stem cell fate. Cell Stem Cell *28*, 1838–1850.e10.

30. Liang, R., Arif, T., Kalmykova, S., Kasianov, A., Lin, M., Menon, V., Qiu, J., Bernitz, J.M., Moore, K., Lin, F., et al. (2020). Restraining Lysosomal Activity Preserves Hematopoietic Stem Cell Quiescence and Potency. Cell Stem Cell *26*, 359–376.e7.

31. Walter, D., Lier, A., Geiselhart, A., Thalheimer, F.B., Huntscha, S., Sobotta, M.C., Moehrle, B., Brocks, D., Bayindir, I., Kaschutnig, P., et al. (2015). Exit from dormancy provokes DNA-damage-induced attrition in haematopoietic stem cells. Nature *520*, 549–552.

32. Wei, Z., and Liu, H.T. (2002). MAPK signal pathways in the regulation of cell proliferation in mammalian cells. Cell Res. *12*, 9–18.

33. Cicenas, J., Zalyte, E., Bairoch, A., and Gaudet, P. (2018). Kinases and Cancer. Cancers *10*, 63.

34. Jacobs, K., Doerdelmann, C., Krietsch, J., González-Acosta, D., Mathis, N., Kushinsky, S., Guarino, E., Gómez-Escolar, C., Martinez, D., Schmid, J.A., et al. (2022). Stress-triggered hematopoietic stem cell proliferation relies on PrimPol-mediated repriming. Mol. Cell *82*, 4176–4188.e8.

35. Doulatov, S., Vo, L.T., Chou, S.S., Kim, P.G., Arora, N., Li, H., Hadland, B.K., Bernstein, I.D., Collins, J.J., Zon, L.I., and Daley, G.Q. (2013). Induction of multipotential hematopoietic progenitors from human pluripotent stem cells via respecification of lineage-restricted precursors. Cell Stem Cell *13*, 459–470.

36. Clien, L., Kostadima, M., Martens, J.H.A., Canu, G., Garcia, S.P., Turro, E., Downes, K., Macaulay, I.C., Bielczyk-Maczynska, E., Coe, S., et al. (2014). Transcriptional diversity during lineage commitment of human blood progenitors. Science *345*, 1251033.

37. Fares, I., Chagraoui, J., Lehnertz, B., MacRae, T., Mayotte, N., Tomellini, E., Aubert, L., Roux, P.P., and Sauvageau, G. (2017). EPCR expression marks UM171-expanded CD34+ cord blood stem cells. Blood *129*, 3344–3351.

38. Velten, L., Haas, S.F., Raffel, S., Blaszkiewicz, S., Islam, S., Hennig, B.P., Hirche, C., Lutz, C., Buss, E.C., Nowak, D., et al. (2017). Human haematopoietic stem cell lineage commitment is a continuous process. Nat. Cell Biol. *19*, 271–281.

39. Popescu, D.M., Botting, R.A., Stephenson, E., Green, K., Webb, S., Jardine, L., Calderbank, E.F., Polanski, K., Goh, I., Efremova, M., et al. (2019). Decoding human fetal liver haematopoiesis. Nature *574*, 365–371.

40. Drissen, R., Buza-Vidas, N., Woll, P., Thongjuea, S., Gambardella, A., Giustacchini, A., Mancini, E., Zriwil, A., Lutteropp, M., Grover, A., et al. (2016). Distinct myeloid progenitor-differentiation pathways identified through single-cell RNA sequencing. Nat. Immunol. *17*, 666–676.

41. Psaila, B., Wang, G., Rodriguez-Meira, A., Li, R., Heuston, E.F., Murphy, L., Yee, D., Hitchcock, I.S., Sousos, N., O'Sullivan, J., et al. (2020). Single-Cell Analyses Reveal Megakaryocyte-Biased Hematopoiesis in Myelofibrosis and Identify Mutant Clone-Specific Targets. Mol. Cell *78*, 477–492.e8.

42. Mende, N., Bastos, H.P., Santoro, A., Mahbubani, K.T., Ciaurro, V., Calderbank, E.F., Quiroga Londoño, M., Sham, K., Mantica, G., Morishima, T., et al. (2022). Unique molecular and functional features of extramedullary hematopoietic stem and progenitor cell reservoirs in humans. Blood *139*, 3387–3401.

43. Lechman, E.R., Gentner, B., van Galen, P., Giustacchini, A., Saini, M., Boccalatte, F.E., Hiramatsu, H., Restuccia, U., Bachi, A., Voisin, V., et al. (2012). Attenuation of miR-126 activity expands HSC in vivo without exhaustion. Cell Stem Cell *11*, 799–811.

44. Sakurai, M., Ishitsuka, K., Ito, R., Wilkinson, A.C., Kimura, T., Mizutani, E., Nishikii, H., Sudo, K., Becker, H.J., Takemoto, H., et al. (2023). Chemically defined cytokine-free expansion of human haematopoietic stem cells. Nature *615*, 127–133.

45. Cabezas-Wallscheid, N., Klimmeck, D., Hansson, J., Lipka, D.B., Reyes, A., Wang, Q., Weichenhan, D., Lier, A., von Paleske, L., Renders, S., et al. (2014). Identification of regulatory networks in HSCs and their immediate progeny via integrated proteome, transcriptome, and DNA methylome analysis. Cell Stem Cell *15*, 507–522.

46. Lauridsen, F.K.B., Jensen, T.L., Rapin, N., Aslan, D., Wilhelmson, A.S., Pundhir, S., Rehn, M., Paul, F., Giladi, A., Hasemann, M.S., et al. (2018). Differences in Cell Cycle Status Underlie Transcriptional Heterogeneity in the HSC Compartment. Cell Rep. *24*, 766–780.

47. Rodriguez-Fraticelli, A.E., Weinreb, C., Wang, S.W., Migueles, R.P., Jankovic, M., Usart, M., Klein, A.M., Lowell, S., and Camargo, F.D. (2020). Single-cell lineage tracing unveils a role for TCF15 in haematopoiesis. Nature *583*, 585–589.

48. Giladi, A., Paul, F., Herzog, Y., Lubling, Y., Weiner, A., Yofe, I., Jaitin, D., Cabezas-Wallscheid, N., Dress, R., Ginhoux, F., et al. (2018). Single-cell characterization of haematopoietic progenitors and their trajectories in homeostasis and perturbed haematopoiesis. Nat. Cell Biol. *20*, 836–846.

49. Wilson, A., Laurenti, E., Oser, G., van der Wath, R.C., Blanco-Bose, W., Jaworski, M., Offner, S., Dunant, C.F., Eshkind, L., Bockamp, E., et al. (2008). Hematopoietic Stem Cells Reversibly Switch from Dormancy to Self-Renewal during Homeostasis and Repair. Cell *135*, 1118–1129.

50. Belluschi, S., Calderbank, E.F., Ciaurro, V., Pijuan-Sala, B., Santoro, A., Mende, N., Diamanti, E., Sham, K.Y.C., Wang, X., Lau, W.W.Y., et al. (2018). Myelo-lymphoid lineage restriction occurs in the human haematopoietic stem cell compartment before lymphoid-primed multipotent progenitors. Nat. Commun. *9*, 4100.

51. Matteini, F., Mulaw, M.A., and Florian, M.C. (2021). Aging of the Hematopoietic Stem Cell Niche: New Tools to Answer an Old Question. Front. Immunol. *12*, 738204.

52. Hammond, C.A., Wu, S.W., Wang, F., MacAldaz, M.E., and Eaves, C.J. (2023). Aging alters the cell cycle control and mitogenic signaling responses of human hematopoietic stem cells. Blood *141*, 1990–2002.

53. Lettera, E., Scala, S., Basso-Ricci, L., Tavella, T., Volpe, L.d., Furno, E.L., Kaufmann, K.B., Garcia-Prat, L., Quaranta, P., Hernandez, R.J., et al. (2023). Molecular and phenotypic blueprint of the hematopoietic compartment reveals proliferation stress as a driver of age-associated human stem cell dysfunctions. bioRxiv. https://doi.org/10.1101/2023.09.15.557553.

54. Ito, K., Hirao, A., Arai, F., Takubo, K., Matsuoka, S., Miyamoto, K., Ohmura, M., Naka, K., Hosokawa, K., Ikeda, Y., and Suda, T. (2006). Reactive oxygen species act through p38 MAPK to limit the lifespan of hematopoietic stem cells. Nat. Med. *12*, 446–451.

55. Johnson, C.S., Williams, M., Sham, K., Belluschi, S., Ma, W., Wang, X., Lau, W.W.Y., Kaufmann, K.B., Krivdova, G., Calderbank, E.F., et al. (2024). Adaptation to ex vivo culture reduces human hematopoietic stem cell activity independently of the cell cycle. Blood *144*, 729–741.

56. Ahuja, A.K., Jodkowska, K., Teloni, F., Bizard, A.H., Zellweger, R., Herrador, R., Ortega, S., Hickson, I.D., Altmeyer, M., Mendez, J., and Lopes, M. (2016). A short G1 phase imposes constitutive replication stress and fork remodelling in mouse embryonic stem cells. Nat. Commun. *7*, 10660.

57. Calvanese, V., Nguyen, A.T., Bolan, T.J., Vavilina, A., Su, T., Lee, L.K., Wang, Y., Lay, F.D., Magnusson, M., Crooks, G.M., et al. (2019). MLLT3 governs human haematopoietic stem-cell self-renewal and engraftment. Nature *576*, 281–286.

58. Zonari, E., Desantis, G., Petrillo, C., Boccalatte, F.E., Lidonnici, M.R., Kajaste-Rudnitski, A., Aiuti, A., Ferrari, G., Naldini, L., and Gentner, B. (2017). Efficient Ex Vivo Engineering and Expansion of Highly Purified Human Hematopoietic Stem and Progenitor Cell Populations for Gene Therapy. Stem Cell Rep. *8*, 977–990.

59. Capo, V., Penna, S., Merelli, I., Barcella, M., Scala, S., Basso-Ricci, L., Draghici, E., Palagano, E., Zonari, E., Desantis, G., et al. (2021). Expanded circulating hematopoietic stem/progenitor cells as novel cell source for the treatment of TCIRG1 osteopetrosis. Haematologica *106*, 74–86.

60. Schiroli, G., Ferrari, S., Conway, A., Jacob, A., Capo, V., Albano, L., Plati, T., Castiello, M.C., Sanvito, F., Gennery, A.R., et al. (2017). Preclinical modeling highlights the therapeutic potential of hematopoietic stem cell gene editing for correction of SCID-X1. Sci. Transl. Med. *9*, eaan0820.

61. Strobel, B., Miller, F.D., Rist, W., and Lamla, T. (2015). Comparative Analysis of Cesium Chloride- and Iodixanol-Based Purification of Recombinant

Adeno-Associated Viral Vectors for Preclinical Applications. Hum. Gene Ther. Methods *26*, 147–157.

62. Gnani, D., Crippa, S., Della Volpe, L., Rossella, V., Conti, A., Lettera, E., Rivis, S., Ometti, M., Fraschini, G., Bernardo, M.E., and Di Micco, R. (2019). An early-senescence state in aged mesenchymal stromal cells contributes to hematopoietic stem and progenitor cell clonogenic impairment through the activation of a pro-inflammatory program. Aging Cell *18*, e12933.
63. Clement, K., Rees, H., Canver, M.C., Gehrke, J.M., Farouni, R., Hsu, J.Y., Cole, M.A., Liu, D.R., Joung, J.K., Bauer, D.E., and Pinello, L. (2019). CRISPResso2 provides accurate and rapid genome editing sequence analysis. Nat. Biotechnol. *37*, 224–226.
64. Nestorowa, S., Hamey, F.K., Pijuan Sala, B., Diamanti, E., Shepherd, M., Laurenti, E., Wilson, N.K., Kent, D.G., and Göttgens, B. (2016). A single-cell resolution map of mouse hematopoietic stem and progenitor cell differentiation. Blood *128*, e20–e31.
65. Korsunsky, I., Millard, N., Fan, J., Slowikowski, K., Zhang, F., Wei, K., Baglaenko, Y., Brenner, M., Loh, P.R., and Raychaudhuri, S. (2019). Fast, sensitive and accurate integration of single-cell data with Harmony. Nat. Methods *16*, 1289–1296.
66. McInnes, L., Healy, J., Saul, N., and Großberger, L. (2018). UMAP: Uniform Manifold Approximation and Projection. J. Open Source Softw. *3*, 861.
67. Wang, G., Wen, W.X., Mead, A.J., Roy, A., Psaila, B., and Thongjuea, S. (2022). Processing single-cell RNA-seq datasets using SingCellaR. STAR Protoc. *3*, 101266.
68. Subramanian, A., Tamayo, P., Mootha, V.K., Mukherjee, S., Ebert, B.L., Gillette, M.A., Paulovich, A., Pomeroy, S.L., Golub, T.R., Lander, E.S., and Mesirov, J.P. (2005). Gene set enrichment analysis: a knowledge-based approach for interpreting genome-wide expression profiles. Proc. Natl. Acad. Sci. USA *102*, 15545–15550.
69. Tirosh, I., Izar, B., Prakadan, S.M., Wadsworth, M.H., 2nd, Treacy, D., Trombetta, J.J., Rotem, A., Rodman, C., Lian, C., Murphy, G., et al. (2016). Dissecting the multicellular ecosystem of metastatic melanoma by single-cell RNA-seq. Science *352*, 189–196.
70. Wilson, N.K., Schoenfelder, S., Hannah, R., Sánchez Castillo, M., Schütte, J., Ladopoulos, V., Mitchelmore, J., Goode, D.K., Calero-Nieto, F.J., Moignard, V., et al. (2016). Integrated genome-scale analysis of the transcriptional regulatory landscape in a blood stem/progenitor cell model. Blood *127*, e12–e23.

STAR★METHODS

KEY RESOURCES TABLE

REAGENT or RESOURCE	SOURCE	IDENTIFIER
Antibodies		
Anti-human CD133/1 PE-Vio 770 (Clone AC133)	Miltenyi Biotec	Cat#130-113-110; RRID: AB_2725939
Anti-human CD34 PE (Clone AC136)	Miltenyi Biotec	Cat#130-113-179; RRID: AB_2726006
Anti-human CD90 APC (Clone 5E10)	BD Biosciences	Cat#559869; RRID: AB_398677
Anti-human CD45 APC-eFluor 780 (Clone HI30)	Invitrogen	Cat#47-0459-42; RRID: AB_1944368
Anti-human CD19 PE (Clone SJ25C1)	BD Biosciences	Cat#345789; RRID: AB_2868815
Anti-human CD13 BV421 (Clone WM15)	BD Biosciences	Cat#562596; RRID: AB_2737672
Anti-human CD3 APC (Clone UCHT1)	BD Biosciences	Cat#555335; RRID: AB_398591
Anti-human CD33 PE-Cy7 (Clone P67.6)	BD Biosciences	Cat#333952; RRID: AB_2713932
Anti-human CD8 PE-Cy7 (Clone RPA-T8)	BD Biosciences	Cat#557746; RRID: AB_396852
Anti-human CD38 PerCP-Cy5.5 (Clone HB-7)	BioLegend	Cat#356614; RRID: AB_2562183
Anti-human CD34 PE-Cy7 (Clone 8G12)	BD Biosciences	Cat#348811; RRID: AB_2868855
Anti-human CD33 BV421 (Clone WM53)	BD Biosciences	Cat#562854; RRID: AB_2737405
Anti-human CD11 b PE (Clone M1/70)	BioLegend	Cat#101207; RRID: AB_312790
Anti-human CD41 PE-Cy5 (Clone HIP8)	BioLegend	Cat#303708; RRID: AB_314378
Anti-human CD45 PE-Cy7 (Clone HI30)	BioLegend	Cat#304016; RRID: AB_314404
Anti-human CD235a (GlyA) APC (Clone GA-R2 (HIR2))	BD Biosciences	Cat#551336; RRID: AB_398499
Anti-human CD14 APC-Cy7 (Clone M5E2)	BioLegend	Cat#301820; RRID: AB_493695
Anti-human CD56 Pacific Blue (Clone MEM-188)	BioLegend	Cat#304629; RRID: AB_2282499
Anti-human CD45Ra Alexa Fluor 700 (Clone HI100)	BioLegend	Cat#304120; RRID: AB_493763
Anti-human CD15 BV510 (Clone W6D3)	BioLegend	Cat#323028; RRID: AB_2563400
Anti-human CD3 PE (Clone OKT3)	BioLegend	Cat#317308; RRID: AB_571913
Anti-human CD19 BV510 (Clone HIB19)	BioLegend	Cat#302242; RRID: AB_2561668
Anti-human CD71 BV421 (Clone CY1G4)	Biolegend	Cat#334122; RRID: AB_2734337
Anti-human CD61 PE-Cy7 (Clone VI-PL2)	Biolegend	Cat#336416; RRID: AB_2566692
Anti-human CD56 PE (Clone AF12-7H3)	Miltenyi Biotec	Cat#130-113-312; RRID: AB_2726090
Anti-human CD45 PerCP-Cy5.5 (Clone 2D1)	Biolegend	Cat#368504; RRID: AB_2566352
Anti-human CD1a APC (Clone HI149)	Biolegend	Cat#300110; RRID: AB_314024
Anti-human CD7 APC-Vio 770 (Clone CD7-6B7)	Miltenyi Biotec	Cat#130-117-677; RRID: AB_2733142
Anti-human CD5 PE-Vio 770 (Clone UCHT2)	Miltenyi Biotec	Cat#130-119-943; RRID: AB_2751939
Anti-human CD34 VioBlue (Clone AC136)	Miltenyi Biotec	Cat#130-095-393; RRID: AB_10827793
Anti-human CD8a APC-H7 (Clone HIT8a)	BD Biosciences	Cat#560179; RRID: AB_1645481
Anti-human TCRα/β PerCP-Cy5.5 (Clone IP26)	Biolegend	Cat#306724; RRID: AB_2563002
Anti-human CD3 APC (Clone REA613)	Miltenyi Biotec	Cat#130-113-135; RRID: AB_2725963
Anti-human CD4 PE-Vio 770 (Clone REA623)	Miltenyi Biotec	Cat#130-113-227; RRID: AB_2726038
Anti-human CD45 Vio Blue (Clone REA747)	Miltenyi Biotec	Cat#130-110-637; RRID: AB_2658243
Anti-human p38-MAPK pThr180/pTyr182	Cell Signaling	Cat#9211; RRID: AB_331641
Anti-8-oxo-2′deoxyguanosine	Trevigen	Cat#4354-MC-050; RRID: AB_1857195
Anti-human FCR Blocking	Miltenyi Biotec	Cat#130059901; RRID: AB_2892112
Purified Rat anti-mouse CD16/CD32 (Clone 2.4G2)	BD Biosciences	Cat#553141; RRID: AB_394656
Donkey anti-mouse IgG (H + L) Secondary Antibody, Alexa Fluor 647	Thermo Fisher Scientific	Cat#A-31571; RRID: AB_162542

(*Continued on next page*)

Continued

REAGENT or RESOURCE	SOURCE	IDENTIFIER
Donkey anti-mouse IgG (H + L) Secondary Antibody, Alexa Fluor 488	Thermo Fisher Scientific	Cat#A-21202; RRID: AB_141607
Donkey anti-rabbit IgG (H + L) Secondary Antibody, Alexa Fluor 568	Thermo Fisher Scientific	Cat#A-10042; RRID: AB_2534017
Mouse anti-human Phospho-Histone H2A.X (Ser139) (Clone JBW301)	Merck Millipore	Cat#05–636; RRID: AB_309864
Rabbit anti-human 53BP1	Bethyl Laboratories	Cat#A300-272A; RRID: AB_185520
Rabbit anti-human phospho-RPA32 (S33)	Bethyl Laboratories	Cat#A300-246A; RRID: AB_2180847
Rabbit anti-human phospho-ATR (Ser428)	Cell Signaling	Cat#2853; RRID: AB_2290281
Rabbit anti-human phospho-CHK1 (Ser345) (Clone 133D3)	Cell Signaling	Cat#2348; RRID: AB_331212
Rabbit anti-human phospho-MAPKAPK-2 (Thr334) (Clone 27B7)	Cell Signaling	Cat#3007; RRID: AB_490936
Rabbit anti-human MAPKAPK-2 (Clone D1E11)	Cell Signaling	Cat#12155; RRID: AB_2797831
Rabbit anti-human phospho-CHK2 (Thr68) (Clone C13C1)	Cell Signaling	Cat#2197; RRID: AB_2080501
Rabbit anti-human Histone H3	Abcam	Cat#ab1791; RRID: AB_302613
Goat anti-rabbit IgG (H + L) Secondary Antibody, HRP	Thermo Fisher Scientific	Cat#31460; RRID: AB_228341
Goat anti-mouse IgG (H + L) Secondary Antibody, HRP	Thermo Fisher Scientific	Cat#31430; RRID: AB_228307
Biological samples		
Umbilical cord blood	San Raffaele Hospital	N/A
Mobilized peripheral blood	Mobilized Leukopak (AllCells)	N/A
Chemicals, peptides, and recombinant proteins		
16,16-Dimethyl Prostaglandin E2	Cayman Chemical	Cat#14750
StemSpan SFEM	STEMCELL Technologies	Cat#09650
MethoCult	STEMCELL Technologies	Cat#H4434
Iscove's DMEM, 1X	Corning	Cat#15-016-CVR
RPMI 1640	Corning	Cat#10-040-CM
B27 supplement	ThermoFisher Scientific	Cat#17504044
L-ascorbic acid 2-phosphate sesqui magnesium salt hydrate	Sigma-Aldrich	Cat#A8960
GlutaMAX™ Supplement	ThermoFisher Scientific	Cat#35050061
Recombinant human stem cell factor (SCF)	Peprotech	Cat#300-07
Recombinant human thrombopoietin (TPO)	Peprotech	Cat#300-18
Recombinant human Flt3-Ligand	Peprotech	Cat#300-19
Recombinant human IL6	Peprotech	Cat#200-06
Recombinant human IL7	Peprotech	Cat#200-07
StemRegenin 1 (SR1)	Biovision	Cat#1967
UM171	STEMCell Technologies	Cat#72914
Human IL-3 recombinant protein	Peprotech	Cat#200-03
Human IL-11	Miltenyi Biotec	Cat#130-103-439
Human GM-CSF	Miltenyi Biotec	Cat#130-093-862
Human IL-2	Miltenyi Biotec	Cat#130097743
Human IL-7	Miltenyi Biotec	Cat#130-095-363
Erythropoietin (EPO, Eprex)	Janssen-Cilag	N/A
Human Low-Density Lipoproteins (LDL)	Stem Cell Technologies	Cat#02698
p38 MAPK inhibitor (SB-203580)	Sigma-Aldrich	Cat#559389

(*Continued on next page*)

Continued

REAGENT or RESOURCE	SOURCE	IDENTIFIER
ERK inhibitor (FR180204)	Sigma-Aldrich	Cat#SML0320
JNK inhibitor (SP600125)	Sigma-Aldrich	Cat#S5567
NAC (N-acetyl-L-cysteine)	Sigma-Aldrich	Cat#A9165
Resveratrol (SRT501)	MedChemExpress	Cat#HY-16561
Tempol (4-Hydroxy-TEMPO)	MedChemExpress	Cat#HY-100561
CDK4/6 inhibitor (Palbociclib-PD0332991)	Selleck Chemicals	Cat#S1116
Cas9 enhancing	Integrated DNA Technologies	Cat#1075916
Alt-R CRISPR-Cas9 tracrRNA	Integrated DNA Technologies	Cat#1072534
Alt-R CRISPR-Cas9 crRNA	Integrated DNA Technologies	http://www.idtdna.com/
Alt-R CRISPR-Cas9 Negative Control crRNA #1	Integrated DNA Technologies	Cat#1072544
SpCas9 Nuclease	Aldevron	Cat#9212
7-AAD Viability Staining solution	Biolegend	Cat#420403
Pacific Blue Annexin V	Biolegend	Cat#640918
CM-H2DCFDA	Thermo Fisher	Cat#C6827
CellROX™ Deep Red Reagent	Thermo Fisher	Cat#C10422
MitoSOX™ Red reagent	Thermo Fisher	Cat#M36008
Intracellular Staining Permeabilization Wash Buffer	Biolegend	Cat#421002
CometAssay Lysis Solution	R&D Systems	Cat#4250-050-01
CometAssay LMAgarose	R&D Systems	Cat#4250-050-02
Poly-L-lysine solution	Sigma-Aldrich	Cat#P8920
Paraformaldehyde solution 4% in PBS	Santa Cruz Biotechnology	Cat#SC-281692
DAPI for nucleic acid staining	Sigma-Aldrich	Cat#D9542
Hoechst 3342 Fluorescent Stain	Thermo Fisher	Cat#62249
Pierce™ Protease and Phosphatase Inhibitor Mini Tablets	Thermo Scientific	Cat#A32961
Critical commercial assays		
QIAamp DNA Micro Kit	QIAGEN	Cat#56304
miRNeasy Micro Kit	QIAGEN	Cat#1071023
RNeasy Plus Micro Kit	QIAGEN	Cat#74034
RNase-free DNase Set	QIAGEN	Cat#79254
iScript cDNA Synthesis Kit	Bio-Rad	Cat#170-8891
P3 Primary Cell 4D-Nucleofector X Kit S	Lonza	Cat#V4XP-3032
Fast SYBR Green Master Mix 2X	Thermo Fisher	Cat#4385618
T7 Endonuclease I	New England Biolabs	Cat#M0302L
iScript cDNA Synthesis Kit	Bio-RAD	Cat#170-8891
TaqMan PreAmp Master Mix 2X	Thermo Fisher	Cat#4488593
Click-iT EdU Alexa Fluor 647 Flow cyometry assay kit	Thermo Fisher	Cat#C10635
Chromium single cell 3′ feature barcode library kit	10X Genomics	Cat#PN-1000079
Seahorse XF Cell Mito Stress Test Kit	Agilent Technologies	Cat#103708-100
Seahorse XF Glycolysis Stress Test Kit	Agilent Technologies	Cat#103020-100
CellTrace™ Violet Cell Proliferation Kit	Thermo Scientific	Cat# C34557
Deposited data		
Raw and analyzed single-cell RNA-seq data	This paper	GEO: GSE238189
Experimental models: cell lines		
Human cord blood CD34^{+} Stem/Progenitor cells	Lonza	Cat#2C-101

(*Continued on next page*)

Continued		
REAGENT or RESOURCE	SOURCE	IDENTIFIER
DLL4-expressing stromal cell line (MS5-hDLL4)	Department of Pathology and Laboratory Medicine, David Geffen School of Medicine, Univ. of California, Los Angeles (UCLA)	N/A
Experimental models: organisms/strains		
NOD.CG- Prkdc^{scid}Il2rg^{tm1Wjl}/SzJ (NSG) *Mus Musculus*	Charles River Laboratories (IACUC: #1385)	RRID: IMSR_JAX:005557
Oligonucleotides		
See Table S1	This paper	N/A
Recombinant DNA		
AAV6.PGK.GFP (AAVS1 HA)	Schiroli et al.[12]	N/A
AAV6.PGK.GFP.bar (AAVS1 HA)	Ferrari et al.[11]	N/A
pCCLsin.PPT.hEF1A-intron.FUCCI.Wpre	Pineda et al.[28]	N/A
Software and algorithms		
BD FACSDiva software	BD Biosciences	https://www.bdbiosciences.com/en-us/products/software/instrument-software/bd-facsdiva-software
Prism software (v8)	GraphPad Prism	https://www.graphpad.com/
QuantaSoft (v1.7)	Biorad	https://www.bio-rad.com/
ImageJ (v2.9)	NIH	https://imagej.nih.gov/ij/
ImageLab (v6)	Bio-Rad	https://www.bio-rad.com/it-it/product/image-lab-software?ID=KRE6P5E8Z
LAS X Leica Software	Leica Mycrosystems	https://www.leica-microsystems.com/it/prodotti/software-per-microscopi/dettagli/product/leica-las-x-ls/
FlowJo	FlowJo	https://www.flowjo.com/
IncuCyte Software S3 (v2018A)	Sartorius	https://www.sartorius.com/en/products/live-cell-imaging-analysis/live-cell-analysis-software/incucyte-s3-software-v2018a?srsltid=AfmBOooK9off6fcxr8aHGCvb8-zK2PlKqZa7PkGJQB6VTRg7V19t5Wd_
Seahorse Wave software (v2.6)	Agilent Technologies	https://www.agilent.com/en/product/cell-analysis/real-time-cell-metabolic-analysis/xf-software/seahorse-wave-controller-software-2-6-1-740904
Code used for the single-cell RNA-seq	This paper	http://www.bioinfotiget.it/gitlab/custom/dellavolpe_geneediting/dellavolpe_scrna-seq.

EXPERIMENTAL MODEL AND STUDY PARTICIPANT DETAILS

Mice

NOD-SCID-IL2Rg$^{-/-}$ (NSG) mice were purchased from Charles River Laboratories and maintained in specific-pathogen-free (SPF) conditions. Specifically, in order to ensure higher transplantation success, engraftment, and better reproducibility, only female mice (8 weeks of age) were used. The procedures involving animals were designed and performed with the approval of the Animal Care and Use Committee of the San Raffaele Hospital and communicated to the Ministry of Health and local authorities according to Italian law (IACUC #1385).

Primary cell cultures

$CD34^+$ HSPCs were either freshly purified from human CB after obtaining informed consent and upon approval by the San Raffaele Hospital ethical committee (TIGET09) or purchased frozen from Lonza. After thawing, HSPCs were seeded at the concentration of 5×10^5 cells/mL in serum-free StemSpan SFEM medium (StemCell Technologies) supplemented with 10μM 16,16-Dimethyl Prostaglandin E2 (added only at thawing) (Cayman), L-glutamine (2mM) and Penicillin-Streptomycin (100 IU/mL penicillin, 100 mg/mL streptomycin), 1μM SR-1 (Biovision), 50nM UM171 (STEMCell Technologies), and human early-acting cytokines (SCF 100 ng/mL, Flt3-L 100 ng/mL, TPO 20 ng/mL, and IL-6 20 ng/mL; Peprotech).

G-CSF or G-CSF + Plerixafor mPB $CD34^+$ HSPCs collected from healthy donors were purified in-house with the CliniMACS CD34 Reagent System (Miltenyi Biotec) from Mobilized Leukopak (AllCells) according to the TIGET-HPCT protocol approved by OSR Ethical Committee and following the manufacturer's instructions. HSPCs were seeded at the concentration of $0.5–1x10^6$ cells/mL in serum-free StemSpan SFEM medium supplemented with 10μM 16,16-Dimethyl Prostaglandin E2 (added only at thawing) (Cayman), L-glutamine (2mM) and Penicillin-Streptomycin (100 IU/mL penicillin, 100 mg/mL streptomycin), 1μM SR-1(Biovision), 35nM UM171 (STEMCell Technologies), and human early-acting cytokines (SCF 300 ng/mL, Flt3-L 300 ng/mL, and TPO 100 ng/mL; Peprotech). All cells were cultured in a 20% O_2 and 5% CO_2 humidified atmosphere at 37°C, except for low-oxygen conditions experiments in which cells were cultured in 3% O_2. Male and female donors were randomly allocated to the experimental groups and the sample size is reported in figure legends for each experiment.

Cell lines

The murine stromal cell line (MS5) edited to ectopically express human Notch ligand, delta-like 4 (hDLL4) was used for the ATO platform and was kindly provided by G.M. Crooks, Department of Pathology and Laboratory Medicine, David Geffen School of Medicine, Univ. of California, Los Angeles (UCLA). hDLL4 cells tested negative for mycoplasma contamination. ATO complete medium is composed by RPMI 1640 (Corning), 4% B27 supplement (ThermoFisher Scientific), 30 μM L-ascorbic acid 2-phosphate sesqui magnesium salt hydrate (Sigma-Aldrich) reconstituted in PBS, 0.2% Primocin (InvivoGen), 100x Glutamax (ThermoFisher Scientific), 5 ng/mL Flt3-L and 5 ng/mL IL-7 (Peprotech).

METHOD DETAILS

In vitro treatments

Where indicated, at day 1 and day 2 post-thawing, HSPCs were treated with 4 or 8μM of p38 inhibitor, 4μM ERK, 2μM JNK inhibitors (SB-203580, FR180204, SP600125; Sigma-Aldrich), 2mM NAC (Sigma-Aldrich) 10μM Resveratrol (Sigma-Aldrich; SRT501), 300μM Tempol (4-Hydroxy-TEMPO, MedChemExpress), or the combination of the three; instead, for CDK4/6 inhibitor (Palbociclib-PD0332991, Selleck Chemicals) administration, HSPCs were treated with 2μM CDK4/6i for 24h before washing out. For all treatments negative control was obtained treating cells with the same volume of DMSO or PBS vehicle.

Gene editing

HSPCs were edited according to a previously optimized protocol[60] after an overnight. or three days of *ex vivo* culture, cells were nucleofected with 2.5–1.25 μM of RNPs and electroporation enhancer (Integrated DNA Technologies) according to manufacturer's instructions using P3 Primary Cell 4D-Nucleofector X Kit and program EO-100 (Lonza). Ribonucleoproteins (RNPs) were assembled by incubating for 10 min at r.t at 1:1.5 M ratio S.p. Cas9 protein (Aldevron) with synthetic gRNAs (Integrated DNA Technologies) targeting *AAVS1* (high specificity) or *IL2RG* locus (low specificity).[12] Transduction with AAV6 was performed at a dose of 1×10^4 vg/cell 15 min after electroporation. AAV6 donor templates for HDR were generated from a construct containing AAV2 inverted terminal repeats, produced by the triple-transfection method, and purified by ultracentrifugation on a cesium chloride gradient as previously described.[61] The design of AAV6 donor templates with homologies for the *AAVS1* locus (encoding for a PGK.GFP reporter cassette) was previously reported.[12] BAR-coded AAV6 was provided by L. Naldini's group.[11]

Colony-forming unit cell assay

CFU-C assay was performed at the indicated timings, plating 800 cells in methylcellulose-based medium (MethoCult H4434, StemCell Technologies) supplemented with 100 IU/mL penicillin and 100 mg/mL streptomycin. Three technical replicates were performed for each sample, and the mean value was plotted and used for statistical analysis. Two weeks after plating, colonies were counted in a blinded fashion, and erythroid, myeloid, and mixed colonies were identified according to morphological criteria.

For the secondary CFU-C assay, one week after seeding primary CFU-C were washed in PBS and 2×10^4 cells were plated for secondary analysis as described above.

Artificial thymic organoid (ATO) system

The ATO platform was generated by A. Villa's group by aggregating 1.5×10^5 DLL4-expressing stromal cell line (MS5-hDLL4) with $7–10 \times 10^3$ CB-derived HSPCs. The resulting cellular suspension was seeded in 0.4 μm Millicell Transwell insert (Millipore) and placed on a 6-well plate containing 1mL of ATO complete medium as previously described.[21]

Single-cell differentiation assay

$CD34^+CD133^+CD45RA^-CD90^+$ population (negative to ZombieAqua viable dye) was sorted as single cells (1 cell/well) and seeded in U-bottom 96-well filled with 100 μL/well Myeloid-Erythroid-Megakaryocyte (MEM) cytokine medium: StemPro medium with nutrients supplement (Life Technologies) supplemented with cytokines (SCF 100 ng/mL, Flt3-L 20 ng/mL, TPO 100 ng/mL, IL-6 50 ng/mL, IL-3 10 ng/mL, all Peprotech; IL-11 50 ng/mL, GM-CSF 20 ng/mL, IL-2 10 ng/mL, IL-7 20 ng/mL; all Miltenyi Biotec), erythropoietin (EPO) 3 units/mL (Eprex, Janssen-Cilag), h-LDL 50 ng/mL (Stem Cell Technologies), 1% L-Glutamine (Life Technologies) and 1% Pen/Strep (Life Technologies). Cells were cultured for 3 weeks in a 5% CO_2 humidified atmosphere at 37°C. Cell sorting was performed on a BD FACSAria Fusion (BD Biosciences) using BDFACS Diva software and equipped with four lasers: blue (488 nm), yellow/green (561 nm), red (640 nm), and violet (405 nm). Cells were sorted with a 100 mm nozzle.

$CD34^+$ HSPC xenotransplantation studies in NSG mice

For primary transplantation, 1 to 2 × 10^5 CB- or 2 × 10^6 mPB-derived $CD34^+$ cells were injected 24h post-editing procedure intravenously into NSG mice after sub-lethal irradiation (150–180 cGy). The sample size was determined by the total number of available treated cells. For secondary transplants, $CD34^+$ cells purified from the BM of primary recipients were pooled according to the experimental group and transplanted in the same number of NSG recipient mice after sub-lethal irradiation (150–180 cGy). Mice were attributed to each experimental group randomly. Human $CD45^+$ cell engraftment and the presence of gene-edited cells were monitored by serial collection of blood from the mouse tail and, at the end of the experiment (15 weeks after transplantation), BM and spleen were harvested and analyzed. Immunophenotypic analyses were conducted as described below.

NHEJ analysis

For molecular analyses, genomic DNA was isolated with QIAamp DNA Micro Kit (QIAGEN). Nuclease activity (*AAVS1* intron 1) was measured by mismatch-sensitive endonuclease assay by PCR-based amplification of the targeted locus followed by digestion with T7 Endonuclease I (NEB) according to the manufacturer's instructions. Digested DNA fragments were resolved and quantified by capillary electrophoresis on LabChip GX Touch HT (PerkinElmer) according to the manufacturer's instructions.

Digital droplet PCR (ddPCR)

Genomic DNA was isolated with QIAamp DNA Micro Kit (QIAGEN). For digital droplet PCR analysis, 5–50 ng of genomic DNA was analyzed using the QX200 Droplet Digital PCR System (Biorad) according to the manufacturer's instructions. Primers and probes were designed between the HDR donor template sequence and the 3′ integration junction on the target AAVS1 locus (listed in Primers and DNA sequences). TTC5 gene was used as the control sequence and the respective primers and probes were purchased in the PrimePCR ddPCR Copy Number Assay: TTC5, Human. The different probes were conjugated with FAM (target) and HEX (TTC5 reference) fluorophores. Thermal conditions for annealing and extension were adjusted as follows: 95°C × 10 min; 94°C × 30 s, 55°C × 1 min, 72°C × 2 min (40 cycles); 98°C × 10 min.

Quantitative PCR (qPCR)

Total RNA was extracted using either miRNeasy Micro Kit (QIAGEN) or RNeasy Plus Micro Kit (QIAGEN), according to the manufacturer's instructions and DNase treatment was performed using RNase-free DNase Set (QIAGEN). For gene expression analyses, cDNA was synthesized with iScript cDNA Synthesis Kit (Bio-Rad), pre-amplified using TaqMan PreAmp Master Mix (ThermoFisher), and used for q-PCR in a Viia7 Real-time PCR thermal cycler using Fast SYBR Green Master Mix (Thermofisher), after standard curve method optimization to reach the 100% primer efficiency for each couple of primers listed in Table S1. Three technical replicates were performed for each sample, and the mean value was selected for further analysis. The relative expression of each target gene was first normalized to *GUSB* housekeeping gene expression and then represented as fold changes ($2^{-\Delta\Delta Ct}$) relative to the indicated control conditions. An RNP loaded with a gRNA with no reported target specificity against the human genome[12] was used as a control for Figure 1C.

Flow cytometry

Immunophenotypic and apoptosis analysis

For immunophenotypic analyses (performed on FACSCanto II; BD Pharmingen) of *ex vivo* cultured HSPCs, cellular suspension (approx. 3–5 × 10^4 cells) was incubated with anti-human FcR Blocking (1:100 dilution) (Miltenyi Biotec) to prevent unwanted binding of antibodies to human Fc receptor-expressing cells. Then, cells were stained with different fluorescent-labeled antibodies (1:100 dilution, each): anti-human CD34 PE (Miltenyi Biotec), anti-human CD133 PE-Vio 770 (Miltenyi Biotec), and anti-human CD90 APC (BD Biosciences). Where indicated immunophenotypic staining was combined with Annexin V (BioLegend) and 7-amino-actinomycin D (7-AAD) (BioLegend) viability staining according to the manufacturer's instructions (3 and 1μL *per* sample, respectively). Apoptosis analysis was performed as previously described.[12]

For immunophenotypic analyses (performed on FACSCanto II; BD Pharmingen) of cells retrieved from *in vivo* organs, we used anti-human and –mouse FcR Blocking (1:100 and 1:200 dilution, respectively) (BD Biosciences) and then cells were stained with different fluorescent-labeled antibodies (1:100 dilution, each).

(1) Peripheral blood: anti-human CD45 APC-eFluor 780, anti-human CD19 PE or BV510, anti-human CD13 BV421, anti-human CD3 APC or PE, anti-human CD33 PE-Cy7 (only at 6w) or anti-human CD8 PE-Cy7 (at 9,12, and 15w);
(2) Bone marrow: anti-human CD45 APC-eFluor 780, anti-human CD90 APC, anti-human CD34 PE-Cy7, anti-human CD19 BV510, anti-human CD13 BV421, and anti-human CD3 PE;
(3) Spleen: anti-human CD45 APC-eFluor 780, anti-human CD19 PE or BV510, anti-human CD13 BV421, anti-human CD3 APC or PE, anti-human CD8 PE-Cy7, anti-human CD71 BV421, anti-human CD235a (GlyA) APC, anti-human CD41 PE-Cy5, and anti-human CD61 PE-Cy7.

Single-stained and Fluorescence Minus One (FMO) stained cells were used as controls and SPHERO Rainbow Calibration Particles (Spherotech) were used to perform instrument calibration. Data were analyzed using the FlowJo software.

Phospho-p38 staining

Cellular suspension (approx. 3–5 × 10^4 cells) was washed with 3 mL of 2% FBS in PBS, eventually stained with surface markers, and fixed with 4% paraformaldehyde (Santa Cruz Biotechnology) at room temperature for 15 min. Cells were washed again with 3 mL of 2% FBS in PBS and permeabilized with 100 μL of 1X Click-iT saponin-based permeabilization at room temperature for 15 min. Then, cells were stained with phospho-p38 MAPK antibody (1:100 dilution) (pThr180/pTyr182; Cell Signaling) at 4°C overnight. After washing with 2% FBS in PBS, samples were stained with anti-rabbit secondary antibodies (1:1000 dilution) (Alexa Fluor 488 or Alexa Fluor 647, Thermo Fisher Scientific) for 45 min at room temperature. After washing with 2% FBS in PBS, sample acquisition was performed on FACSCanto II and the collected data were analyzed using the FlowJo software.

MEM single-cell differentiation assay analysis

All single-cell-derived colonies were harvested into 96 U-bottom plates. Cells were then stained with 50 μL/well of antibody mix (CD45-PECy7, CD11b-PE, CD41-PECy5, GlyA-APC, CD14-APCCy7, CD56-BV421, CD15-BV510, 1:300, 1:500, 1:200, 1:1000, 1:500, 1:200, 1:1000, respectively), incubated for 20 min in the dark at room temperature and then washed with 100 μL/well of 1xDPBS +2% FBS. The type (lineage composition) and the size of the colonies formed were assessed by high-throughput flow cytometry. A single cell was defined as giving rise to a colony if the sum of cells detected in the $CD45^+$ gates was ≥30 cells. Erythroid (Ery) colonies were identified as $CD45^-GlyA^+ \geq 30$ cells, Megakaryocytes (Meg) colonies as $CD45^+CD41^+ \geq 30$ cells, Myeloid (My) colonies as [Monocytes (Mono: $CD45^+CD14^+$) + Granulocytes (Gran: $CD45^+CD15^+$)] ≥ 30 cells, and NK colonies as $CD45^+CD56^+ \geq 30$ cells.

Artificial thymic organoid (ATO) analysis

After five weeks from seeding, ATOs were collected by adding MACS Buffer (Miltenyi Biotech) to each well and pipetting to dissociate the ATOs. Cells were then filtered with a 70 μm filter, counted, and stained with 100ul/tube of of T cell progenitor antibody mix (CD56-PE, CD45-PerCP-Cy5, CD1a-APC, CD7-APCH7, CD5-PECy7, CD34-VB, LiveDead-PO; 1:100 dilution, respectively) and mature T cell antibody mix (CD8a-APC-Vio770, TCRab-PerCP-Cy5.5, CD56-PE, CD3-APC, CD4-PE-Vio770, CD45-VB, LiveDead-PO; 1:100 dilution, respectively). Cells were incubated for 15 min at room temperature and then washed with 1mL/tube of 2% FBS in PBS. Absolute number of $TCRa/b^+$ cells was calculated from cell counts and percentage of positive cells from FACS analyses. Frequency of GFP^+ cells was gated on $CD56^-CD45^+$ cells. Sample acquisition was performed on FACSCanto II and the collected data were analyzed using the FlowJo software.

CM-H_2DCFDA and CellROX

CM-H_2DCFDA (Thermo Fisher Scientific) was dissolved in DMSO. This molecule passively diffuses into cells, subsequent oxidation yields a fluorescent adduct that is trapped inside the cell. Cells were resuspended in pre-warmed 1x DPBS and a 10 μM probe was added. After 30 min in the incubator at 37°C, cells were centrifuged and resuspended in pre-warmed 1xDPBS +2% FBS. Fluorescence was quickly acquired at FACSCanto II using excitation sources and filters appropriate for fluorescein (FITC) and the collected data were analyzed using the FlowJo software. Because the dye is susceptible to photo-oxidation, all the steps were performed in the dark.

When CM-H_2DCFDA was not compatible with the experimental conditions, ROS levels were analyzed using the CellROX Reagents (Thermo Fisher) according to the manufacturer's instructions. In detail, cells were incubated with 500nM CellROX Reagent for 60 min at 37°C protected from light.

MitoSOX red mitochondrial superoxide indicator

MitoSOX Red reagent (Thermo Fisher Scientific) permeates live cells and selectively targets mitochondria. It is rapidly oxidized by superoxide but not by other ROS and reactive nitrogen species (RNS). The oxidized product becomes highly fluorescent (Ex/Em 510/580) upon binding to nucleic acid. MitoSOX Red reagent was dissolved in DMSO and 5μM were directly added to the cell culture. Cells were incubated for 10 min at 37°C protected from light. After washing in 1xDPBS +2% FBS, fluorescence was quickly acquired at FACSCanto II and the collected data were analyzed using the FlowJo software.

8-Oxo-2′-deoxyguanosine staining

Cellular suspension (approx. 1.5×10^5 cells) was washed with 3 mL of 2% FBS in PBS and fixed with 4% paraformaldehyde (Santa Cruz Biotechnology) at room temperature for 15 min. Cells were washed again with 3 mL of 2% FBS in PBS and denatured with 100 μL of HCl (2N) at room temperature for 20 min. After washing with 2% FBS in PBS, cells were permeabilized with 800 μL of 1X Intracellular Staining Permeabilization Wash Buffer (BioLegend) at room temperature for 20 min. Then, cells were washed with 2% FBS in PBS and stained with 8-oxo-2′-deoxyguanosine Antibody (1:250 dilution) (Trevigen) at 4°C overnight. After washing

with 2% FBS in PBS, samples were stained with anti-mouse secondary antibody Alexa Fluor 488 (1:1000 dilution) (Thermo Fisher Scientific) for 45 min at room temperature. Cells were washed with 2% FBS in PBS and sample acquisition was performed on FACSCanto II and the collected data were analyzed using the FlowJo software.

Immunofluorescence analysis

Multitest slides (10 well, MP Biomedicals) were treated for 20 min with Poly-L-lysine solution (Sigma-Aldrich) at 1 mg/mL concentration. After two washes with DPBS solution, approximately 0.3/0.5 × 10^5 cells were seeded on covers for 20 min and fixed with 4% paraformaldehyde (Santa Cruz Biotechnology) for another 20 min. Cells were then permeabilized with 0.3% Triton X-100. After blocking with 0.5% BSA and 0.2% fish gelatin in DPBS, cells were probed with the indicated primary antibodies. After primary antibodies incubation (53BP1 Antibody, Bethyl Laboratories, 1:600 dilution; Anti-phospho Histone H2A.X (Ser139) Antibody, clone JBW301, Merk, 1:200 dilution; and phospho-RPA32 (S33) Antibody, Bethyl Laboratories, 1:200 dilution), cells were washed three times with DPBS and incubated with Alexa 488-, 568- and/or 647-labeled secondary antibodies (1:1000 dilution) (Thermo Fisher Scientific). Nuclear DNA was stained with DAPI (Sigma-Aldrich) and covers were mounted with Aqua-Poly/Mount solution (Polysciences. Inc.) on glass slides (Bio-Optica). Fluorescent images were acquired using Leica SP5 Confocal microscope and analyses of 53BP1 foci distribution, and γH2A.X and pRPA positive cells. Micronuclei quantifications were performed with ImageJ software on DAPI images.

Comet assay

HSPCs were suspended at 1 × 10^5 cells/mL in ice-cold 1xDPBS and mixed with molten Comet LMAgarose (Trevigen, MD) at a ratio of 1:10 (v/v) and immediately pipetted onto CometSlides (Trevigen, MD) and placed for 30 min at +4°C. Once solidified, the slides were immersed in pre-chilled Lysis Solution (Trevigen, MD) for 1 h at +4°C. Following lysis, slides were immersed in freshly prepared Alkaline Unwinding Solution pH > 13 (300 mM NaOH, 1mM EDTA) for 1 h at +4°C and then electrophoresed in Alkaline Electrophoresis Solution pH > 13 (300 mM NaOH, 1mM EDTA) at 300 mA for 40 min. Slides were washed twice in ddH2O and fixed in 70% ethanol for 5 min. Comets were stained with SYBR Safe (Invitrogen) at room temperature for 30 min. All steps were conducted in the dark to prevent additional DNA damage. Comets were analyzed using a Nikon Eclipse E600 microscope and a Nikon-DS-RI2 camera. At least 100 nuclei for each donor were analyzed with CaspLab software to determine the "Olive Tail Moments" of individual nuclei.

Seahorse metabolic flux analysis

Metabolic flux analyses were performed using the Seahorse XFe96 Analyzer according to the manufacturer's instructions. Briefly, an XF sensor cartridge was hydrated overnight in Seahorse XF Calibrant at 37°C in a non-CO_2 incubator. Then, a cell culture microplate was coated for 30 min with Cell-Tak diluted in sodium carbonate 0.1 M pH8 and washed twice with dH_2O. CB-derived HSPCs (about 10^5 cells) were resuspended in freshly made Seahorse XF RPMI medium (pH 7.4; supplemented according to the desired stress test to perform), seeded in a 96-well Seahorse cell culture microplate, centrifuged for 15 min at 1500 rpm, and incubated in the 37°C incubator in absence of CO_2 for 1 h. Six technical replicates were performed for each sample, and the mean value was selected for further analysis.

Oxygen Consumption Rate (OCR) was measured using the Seahorse XF Mito Stress Test Kit. Cells were sequentially treated with 1 μM oligomycin (port A), 4 μM carbonyl cyanide-4 (trifluoromethoxy) phenylhydrazone (FCCP) (port B) and 0.5 μM antimycin A/rotenone (port C). Measurements were conducted using the following settings: 5 min mix time and 9 min read time.

Extracellular Acidification Rate (ECAR) was measured using the Seahorse XF Glycolysis Stress Test Kit. Cells were sequentially treated with 10 mM Glucose (port A), 1 μM oligomycin (port B), and 50 mM 2-deoxy-glucose. Measurements were conducted using the following settings: 5 min mix time and 9 min read time.

Analyses were performed with the Agilent Seahorse Wave software (Agilent Technologies). OCR and ECAR values were normalized on the total number of cells per well; cell numbers were calculated using CyQuant Cell Proliferation Assay (Thermo Fisher Scientific).

Western blot

To prepare protein extracts for immunoblot analysis, cells were washed twice with cold PBS and lysed for 30 min on ice with RIPA buffer containing 50 mM Tris–HCl pH 8.0, 150 mM NaCl, 1% (v/v) NP-40, 0.5% (w/v) Sodium Deoxycholate, 1 mM EDTA, 0.1% (w/v) SDS, 0.01% (w/v) Sodium azide pH 7.4, and Pierce protease and phosphatase minitablets inhibitors (Thermo Fisher Scientific, A32961). Cells were centrifuged at 13,000 rpm at 4 °C for 10 min and the supernatants were quantified for protein content with Pierce's BCA protein assay kit (Thermo Fisher Scientific, 23227), according to manufacturer's instructions. Then, the extracted proteins were resolved by SDS–PAGE before transfer onto nitrocellulose membrane (Sigma-Aldrich, GEH10600003), followed by overnight incubation at 4°C with phospho-ATR (Ser428) (Cell Signaling, 2853, 1:250 dilution), phospho-CHK1 (Ser 345) (Cell Signaling, 2341, 1:500 dilution), phospho-CHK2 (Thr68) (Cell Signaling, 2661, 1:1000 dilution), phospho-MAPKAPK-2 (Thr334) (Cell Signaling, 3007, 1:500 dilution), MAPKAPK-2 (Cell Signaling, 3042, 1:1000 dilution) and Histone 3 (Abcam, AB1791, 1:1000 dilution) primary antibodies. Finally, membranes were incubated 1h at room temperature with an anti-rabbit or anti-mouse HRP-linked secondary antibodies (Thermo Fisher Scientific, 1:3000 and 1:2000 dilution, respectively) and signals were detected using ECL Western blotting substrate (Thermo Fisher Scientific, 32209) following the recommendations of the manufacturer's instructions. The images were acquired on a ChemiDoc imager (BioRad).

EdU incorporation and detection for flow cytometry

EdU (5-ethynyl-2′-deoxyuridine), supplied with Click-iT EdU Alexa Fluor 647 Imaging Kit (Thermo-Fisher Scientific), was diluted in DMSO to a final concentration of 10 mM and kept at −20°C. Cells were treated with 2μM EdU for 4 h in culture. Approximately 3–5 × 10^4 cells were washed with 3 mL of 1% BSA in PBS and fixed with 100 μL of Click-iT fixative for 15 min. Cells were washed again with 3 mL of 1% BSA in PBS and permeabilized with 100 μL of 1X Click-iT saponin-based permeabilization for 15 min. Detection of EdU-DNA was performed by incubating cells with 500 μL of Click-iT Plus reaction cocktail for 30 min at room temperature protected from light. Cells were subsequently washed with 3 mL of 1% BSA in PBS before staining DNA with 2μM Hoechst 33342 for o.n. at 4°C protected from light. After the incubation, sample acquisition was performed on FACSymphony A5 SORP (BD Biosciences), and the collected data were analyzed using the FlowJo software.

Live imaging analysis of confluency

IncuCyte (Essen Biosciences) was used to quantify confluency in live cells for 4 days 30.000 cells of each condition were plated in a 96-multiwell placed in an incubator to maintain the standard cell culture conditions (5% CO_2 humidified atmosphere at 37°C) and images were acquired each 15'. The confluence processing analysis tool (IncuCyte Software S3 v2018A) calculated confluency for each sample. Quantification of the cellular confluence of each condition was assessed by calculating fold change to the first time point.

Cell trace violet

Just after thawing, HSPCs were stained with Cell Trace Violet (Thermo Scientific, C34557) following the manufacturer's instructions. Cells were resuspended in 1xDPBS at a concentration of 10^6/mL and 1μL of Cell Trace solution was added per each mL of cell suspension for a final concentration of 5μM. Cells were incubated for 20 min at 37°C, protected from light, and then for 5 min with five times the original staining volume of 1xDPBS+2% FBS. After centrifugation, cells were resuspended in the appropriate culture medium volume and incubated for at least 30 min before the analysis. Samples acquisition was performed on FACSCanto II and the collected data were analyzed with the FlowJo software using the Proliferation Kinetics tool.

Cell cycle analyses with the Fucci2a system

Lentiviral Fucci2A expressing vector was generated as previously described.[62] The day after thawing, HSPCs were treated with DMSO, 2mM NAC, or 4μM p38 inhibitor and 12h later transduced at a multiplicity of infection (MOI) of 50 for 16h. On day 2, cells were treated with the second dose of NAC, p38 inhibitor, or DMSO, and the day after were counted and seeded at a density of 20.000 cells in a 96-well plate. Transduced cells were monitored with IncuCyte (Essen Biosciences) for 4 days and time-lapse imaging was acquired taking phase contrast, red and green fluorescent signal recording images each 30 min. Cell cycle kinetics of transduced HSPCs were analyzed by tracking single cells throughout animation and single measurements were made using analysis tools Pixel Inspection of ImageJ. The average red and green fluorescence intensity was recorded from every cell. Specifically, we took at least 5 completed cell cycle phases for the comparison between treatments. Cell cycle kinetics were determined by plotting the duration of red, green, or yellow fluorescence intensity over time using Prism software v5 (GraphPad Software Inc.).

BAR- and indels-based clonal tracking libraries

Library preparation was performed as previously described.[11] Briefly, for BAR-Seq library preparation: we analyzed only mice transplanted with HS + AAV6-edited HSPCs with detectable engraftment (>0.1%) of GFP^+ cells in the BM at 15 weeks. PCR amplicons for individual samples were generated by nested PCR using primers listed in Ferrari et al., 2020 and starting from >50 to 100 ng of purified gDNA. The first PCR step was performed with GoTaq G2 DNA Polymerase (Promega) according to the manufacturer's instructions using the following amplification protocol: 95°C for 5 min, (95°C for 0.5 min, 60°C for 0.5 min, 72°C for 0.5 min) × 20 cycles, 72°C for 5 min. Forward primer was designed to bind the donor template upstream of the BAR sequence, while the reverse primer annealed outside the homology arm, thus amplifying 328 bp of the on-target integrated cassette. For targeted deep sequencing of the plasmid and AAV libraries, the reverse primer was annealed to the homology arm. The second PCR step was performed with GoTaq G2 DNA Polymerase (Promega) according to the manufacturer's instructions using 5 μL of the first-step PCR product and the following amplification protocol: 95°C for 5 min, (95°C for 0.5 min, 60°C for 0.5 min, 72°C for 0.5 min) × 20 cycles, 72°C for 5 min. Second-step PCR primers were endowed with tails containing P5/P7 sequences, i5/i7 Illumina tags to allow multiplexed sequencing, and R1/R2 primer binding sites. PCR amplicons were separately purified using the MinElute PCR Purification kit (QIAGEN) and AmpPure XP beads (Beckman Coulter). Library quality was assessed by Agilent Tapestation (Agilent Technologies). Amplicons were multiplexed and run on MiSeq 2 × 75 bp or 2 × 150 bp paired-end (Illumina). Indels-based clonal tracking library preparation: PCR amplicons for individual samples were generated by nested PCR using primers listed in *Ferrari* et al*., 2020* and starting from >50 to 100 ng of purified gDNA. The first PCR stepwas performed with GoTaq G2 DNA Polymerase (Promega) according to the manufacturer's instructions using the following amplification protocol: 95°C for 5 min, (95°C for 0.5 min, 60°C for 0.5 min, 72°C for 0.25 min) × 20 cycles, 72°C for 5 min. The second PCR step was performed with GoTaq G2 DNA Polymerase (Promega) according to the manufacturer's instructions using 5 μL of the first-step PCR product and the following amplification protocol: 95°C for 5min; 95°C × 0.5 min, 60°C × 0.5 min, 72°C × 0.3 min, (20cycles); 72°Cx 5 min. Second-step PCR primers were endowed with tails containing P5/P7 sequences, i5/i7 Illumina tags to allow multiplexed sequencing, and R1/R2 primer binding sites. PCR amplicons were separately purified

performing double-side selection with AmpPure XP beads (Beckman Coulter). Library quality was assessed by LabChip GX Touch HT (PerkinElmer). Amplicons were multiplexed and sequenced by GeneWiz on MiSeq 2 × 300 bp paired-end sequencing (Illumina).

BAR-seq analysis

Barcoded samples were analyzed with the BAR-Seq2 pipeline (https://bitbucket.org/bereste/bar-seq2). In detail, input reads were pre-processed to get rid of low-quality bases and keep sequences having lengths ≥120bp (options: -m 120 -q 30) to ensure having the entire amplicon within each read. Barcodes (BARs) were then extracted using TagDust (by providing the amplicon structure) and corrected using a community-based strategy on a graph built on sequence similarity (edit distance ≤2). Resulting BARs were quantified based on their abundance (number of supporting reads) and filtered, keeping only those having a count greater than 2. Samples having a low number of extracted barcodes (<15000) were discarded from the analysis.

Indels-based clonal tracking analysis

Samples for indels-based clonal tracking were analyzed with CRISPResso2 (v2.2.8),[63] a suite of software developed to detect and quantify insertions, mutations, and deletions in reads from gene editing experiments. In details, input sequences were trimmed (CRISPResso2 options: –trim_sequences –trimmomatic_command trimmomatic –trimmomatic_options_string 'ILLUMINACLIP:TruSeq3-PE-2.fa:2:30:10 MINLEN:100′) to get rid of low-quality positions (score <30) and to remove Illumina adapters, keeping only trimmed reads having length greater than 100bp to ensure the full coverage of the region of interest. Then, the resulting sequences were mapped to the reference amplicon and a quantification window around the cut site (identified through the provided gRNA) was set to identify all the occurred events. The computed alleles were quantified by measuring the number of reads and their relative abundance based on total read counts. Finally, CRISPResso2 output alleles were post-processed by correcting all the mismatch positions outside the quantification window and re-quantifying the total read counts and consequently, the corresponding relative abundances, filtering out those having a relative abundance lower than the false positive threshold (set at 0.2%, based on untreated controls).

Single-cell RNA-sequencing and analysis

Droplet-based digital 3′-end scRNA-Seq was performed on a Chromium Single-Cell Controller (10X Genomics) using the Chromium Next GEM Single Cell 3′ Reagent Kit v3.1 according to the manufacturer's instructions. 24h after the editing treatment, viable $CD34^+$ cells (negative to ZombieAqua viable dye) were sorted according to surface expression of $CD34^+CD133^+CD45RA^-CD90^+GFP^+$ and $CD34^+CD133^+CD45RA^-CD90^+GFP^-$. Cell sorting was performed on a BD FACSAria Fusion (BD Biosciences) using BDFACS Diva software and equipped with four lasers: blue (488 nm), yellow/green (561 nm), red (640 nm), and violet (405 nm). Cells were sorted with a 100 mm nozzle. A highly pure sorting modality (two-way purity sorting) was chosen. Sorted cells were collected in 1.5 mL Eppendorf tubes containing 100 μL of 1xDPBS. The sorted populations were stained for 30′ at 4°C with Total Seq-B hashtag antibodies (Data S1F, H1 for $Zombie^-$ not edited DMSO and p38i, Hs Cas9 DMSO and p38i, and for $Zombie^-GFP^+$ HS + AAV6 DMSO and p38i; H2 for $Zombie^-$ not edited DMSO and p38i, Hs Cas9 DMSO and p38i, and for $Zombie^-GFP^-$ HS + AAV6 DMSO and p38i; H3 for $CD34^+CD133^+CD45RA^-CD90^+GFP^+$ HS + AAV6 DMSO and p38i; H4 for $CD34^+CD133^+CD45RA^-CD90^+GFP^-$ HS + AAV6 DMSO and H5 for $CD34^+CD133^+CD45RA^-CD90^+GFP^-$ HS + AAV6 p38i), and after pooling population from the same condition, viable cells were counted with Trypan Blue solution 0.4% (GIBCO) and 1,2–5 × 10^4 viable cells from each population were utilized for the subsequent procedure (estimated recovery: 3 × 10^4 cells/sample). Briefly, single cells were partitioned in Gel Beads in Emulsion (GEMs) and lysed, followed by RNA barcoding, reverse transcription, and PCR amplification (11 cycles). scRNA-Seq libraries were prepared according to the manufacturer's instructions, checked, and quantified on LabChip GX Touch HT (PerkinElmer) and Qubit 3.0 (Invitrogen) instruments. Sequencing was performed on a Nova Seq S2 (Illumina) using the NextSeq 500/550 High Output v2 kit (75 cycles).

Illumina sequencer's base call files (BCLs) were demultiplexed, for each flow cell directory, into FASTQ files using Cellranger mkfastq with default parameters (v. 6.1.1, https://github.com/10XGenomics/cellranger). FASTQ files of both genome expression (GEX) and hashtags (HTO) for each sample were then processed together using Cellranger count with default parameters, to obtain quantification of cells (in terms of UMI counts) on genes and hashtags. Internally, the software relies on STAR for aligning reads to the human reference genome (GRCh38) that was modified to include the insertion of the GFP gene in the AAVS1 locus. The output of CellRanger was analyzed in the R environment with the Seurat (v4.1.1) package, keeping cells having more than 200 and fewer than 6000 unique genes per cell, and genes expressed in more than 3 cells. Moreover, cells with more than 15% of features mapping to mitochondrial genes were excluded. HTO data of each sample were normalized with a centered log-ratio (CLR) transformation across features, and cell demultiplexing was performed for each sample with the HTODemux function from Seurat (positive.quantile = 0.9). Finally, only cells with a unique hashtag (singlet) identifying a sorted population were retained. Samples were merged together, obtaining a total of 102842 cells passing the quality check, with an average of ∼3826 genes per cell and ∼14973 UMIs/reads per cell. Counts were then normalized using the NormalizeData function with default parameters. Cell cycle scores were calculated using the CellCycleScoring function, providing as input a previously reported gene list.[64] Expression data were then scaled using the ScaleData function, also regressing on the cell cycle phases (S, G2M scores as calculated with the CellCycleScoring function), on the percentage of mitochondrial genes, and the total number of reads per cell.

After that, Principal Component Analysis (PCA) was performed using the RunPCA function, providing as input a list of the top 20% most variable genes (*vst* method in FindVariableFeatures function). To correct for the gender bias, that was extreme in the HSC compartment, a variable based on the XIST expression (XIST>0 for female, otherwise male) was created, and a batch correction based on this latter classification, as well as on the sample origin was performed with Harmony.[65] Cell clusters were defined by evaluating the first 50 principal components at a resolution of 2 and using the FindClusters function with standard parameters. Cells were visualized in 2 dimensions using UMAP (Uniform Manifold Approximation and Projection).[66] Genes enriched in cells within each cluster were identified by means of the Wilcoxon rank-sum test (FindAllMarkers function), selecting genes expressed in at least 20% of one of the two populations (min.pct = 0.2). For the cluster annotation, similarly to what has been published,[67] marker genes identified for each cluster were used to perform a pre-ranked GSEA[68] on signature lists from literature.[35–42,69] We annotated 15 cell clusters, including HSC/multi-potent progenitor (MPP), MPP, lympho-multi potent progenitors (LMPP), lymphoid progenitors (LyP), a small subset of pro-B progenitor cells, more committed progenitors as granulocyte-monocyte progenitors (GMP), monocyte-dendritic progenitors (MDP), megakaryocytes-erythroid progenitors (MEP), megakaryocyte erythroid mast cell and basophil progenitors (MEMBP), eosinophil baso-mast progenitors (EBMPs), megakaryocyte erythroid baso-mast progenitors (MEP_Baso_Mast) and Erythroid progenitor (EryP) (Data S1G). Once cluster annotation was defined, genes differentially expressed between different conditions/clusters were identified using the FindMarkers function, applying the Wilcoxon test and the default correction method (Bonferroni). For the functional annotation, differentially expressed genes were pre-ranked according to Log2FC values and GSEA was performed on MSigDB (http://www.gsea-msigdb.org/gsea/msigdb/collections.jsp), Gene Ontology biological processes (GO:BP), the Pathway Interaction Database, and literature available human and murine datasets. Specifically, the human signatures derived from García-Prat et al. 2021 and Cabezas-Wallscheid et al. 2014-17[29,45] identify HSC and dormant HSC (dHSC) signatures. Jacobs et al.[34] identify DNA replication stress signatures in HSCs. Lauridsen et al. 2018[46] dHSC signature is derived from the comparison of an HSC population with low expression of Retinoic Acid-CFP reported, which is a non-proliferative population displaying superior engraftment potential, vs. Retinoic Acid-CFP bright HSCs. Giladi et al. 2018[48] StemScore derived from a population of HSCs with high Hlf expression. Wilson et al. 2016[70] signatures derived from single-cell data of sorted LT-HSCs, expressing a gene program relative to a low cell cycle. Rodriguez-Fraticelli et al. 2020[47] identifies 4 different clusters of HSCs, 1–2 retaining a more stem signature, while clusters 3–4 are characterized by a more active cellular state and Mk priming respectively. Furthermore, Rodriguez-Fraticelli et al. 2020[47] characterizes HSC heterogeneity by low/high and lineage bias output of HSC clones detected by means of a barcoding strategy.

The AddModuleScore function was adopted to compute the average expression level of cell programs. Wilcoxon rank sum was adopted to test pairwise the differences across conditions, correcting the *p*-value with the Benjamini-Hochberg correction method.

QUANTIFICATION AND STATISTICAL ANALYSIS

Measurements were taken from distinct samples and sample size (n) is reported in the figure legends. Inferential techniques were carried out whenever an appropriate sample size was available; otherwise, descriptive statistics were reported. Mann-Whitney test was performed to compare two independent groups. In the presence of more than two independent groups, the Kruskal-Wallis test was performed, followed by post hoc pairwise comparisons. For paired observations, the Wilcoxon matched-pairs signed rank test was performed. For WB analysis, one-sample T-test was performed on normalized data. All tests were performed with two-tail statistics. Data were analyzed using Prism software v8 (GraphPad Software Inc.). Values are expressed as means ± SD or SEM as indicated. p values < 0.05 were considered significant (*, $p < 0.05$; **, $p < 0.01$; ***, $p < 0.001$; ****, $p < 0.0001$).